Discovery of a Little Red Dot Candidate at $z \gtrsim 10$ in COSMOS-web Based on MIRI-NIRCam Selection

Takumi S. Tanaka[1,2,3], Hollis B. Akins[4], Yuichi Harikane[5], John D. Silverman[1,2,3], Caitlin M. Casey[4,6,7], Kohei Inayoshi[8], Jan-Torge Schindler[9], Kazuhiro Shimasaku[2,10], Dale D. Kocevski[11], Masafusa Onoue[1,12,13], Andreas L. Faisst[14], Brant E. Robertson[15], Vasily Kokorev[16], Marko Shuntov[7,17,18], Anton M. Koekemoer[19], Maximilien Franco[20], Eiichi Egami[21], Daizhong Liu[22], Anthony J. Taylor[23], Jeyhan S. Kartaltepe[24], Sarah E. I. Bosman[25,26], Jaclyn B. Champagne[27], Koki Kakiichi[7,17], Santosh Harish[24], Zijian Zhang[8,28], Sophie L. Newman[29], Darshan Kakkad[30], Qinyue Fei[31], Seiji Fujimoto[23,31,32], Mingyu Li[33], Steven L. Finkelstein[23], Zi-Jian Li[34,35], Erini Lambrides[36], Laura Sommovigo[37], Jorge A. Zavala[38], Kei Ito[7,39], Zhaoxuan Liu[1,2,3], Ezequiel Treister[40], Manuel Aravena[41,42], Ghassem Gozaliasl[43,44], Haowen Zhang[27], Hossein Hatamnia[45], Hiroya Umeda[5,46], Akio K. Inoue[47,48], Jinyi Yang[49], Makoto Ando[50], Junya Arita[2], Xuheng Ding[51], Suin Matsui[2], Yuki Shibanuma[2], Georgios Magdis[7,17,39], Mingyang Zhuang[52], Xiaohui Fan[27], Zihao Li[7,53], Weizhe Liu[27], Jianwei Lyu[27], Jason Rhodes[54], Sune Toft[7,17], Feige Wang[49], Siwei Zou[55,56], Rafael C. Arango-Toro[57], Andrew J. Battisti[58,59], Steven Gillman[7,39], Ali Ahmad Khostovan[24,60], Arianna S. Long[61], Bahram Mobasher[45], and David B. Sanders[62]

[1] Kavli Institute for the Physics and Mathematics of the Universe (WPI), The University of Tokyo Institutes for Advanced Study, The University of Tokyo, Kashiwa, Chiba 277-8583, Japan; takumi.tanaka@ipmu.jp
[2] Department of Astronomy, Graduate School of Science, The University of Tokyo, 7-3-1 Hongo, Bunkyo-ku, Tokyo 113-0033, Japan
[3] Center for Data-Driven Discovery, Kavli IPMU (WPI), UTIAS, The University of Tokyo, Kashiwa, Chiba 277-8583, Japan
[4] The University of Texas at Austin, 2515 Speedway Boulevard Stop C1400, Austin, TX 78712, USA
[5] Institute for Cosmic Ray Research, The University of Tokyo, 5-1-5 Kashiwanoha, Kashiwa, Chiba 277-8582, Japan
[6] Department of Physics, University of California, Santa Barbara, Santa Barbara, CA 93106, USA
[7] Cosmic Dawn Center (DAWN), Denmark
[8] Kavli Institute for Astronomy and Astrophysics, Peking University, Beijing 100871, People's Republic of China
[9] Hamburger Sternwarte, University of Hamburg, Gojenbergsweg 112, D-21029 Hamburg, Germany
[10] Research Center for the Early Universe, Graduate School of Science, The University of Tokyo, 7-3-1 Hongo, Bunkyo-ku, Tokyo 113-0033, Japan
[11] Department of Physics and Astronomy, Colby College, Waterville, ME 04901, USA
[12] Waseda Institute for Advanced Study (WIAS), Waseda University, 1-21-1, Nishi-Waseda, Shinjuku, Tokyo 169-0051, Japan
[13] Center for Data Science, Waseda University, 1-6-1, Nishi-Waseda, Shinjuku, Tokyo 169-0051, Japan
[14] Caltech/IPAC, MS 314-6, 1200 E. California Boulevard, Pasadena, CA 91125, USA
[15] Department of Astronomy and Astrophysics, University of California, Santa Cruz, 1156 High Street, Santa Cruz, CA 95064, USA
[16] Kapteyn Astronomical Institute, University of Groningen, PO Box 800, 9700 AV Groningen, The Netherlands
[17] Niels Bohr Institute, University of Copenhagen, Jagtvej 128, DK-2200, Copenhagen, Denmark
[18] University of Geneva, 24 rue du Général-Dufour, 1211 Genève 4, Switzerland
[19] Space Telescope Science Institute, 3700 San Martin Drive, Baltimore, MD 21218, USA
[20] Université Paris-Saclay, Université Paris Cité, CEA, CNRS, AIM, 91191 Gif-sur-Yvette, France
[21] Steward Observatory, University of Arizona, 933 N. Cherry Avenue, Tucson, AZ 85721, USA
[22] Purple Mountain Observatory, Chinese Academy of Sciences, 10 Yuanhua Road, Nanjing 210023, People's Republic of China
[23] Department of Astronomy, The University of Texas at Austin, 2515 Speedway, Austin, TX, 78712, USA
[24] Laboratory for Multiwavelength Astrophysics, School of Physics and Astronomy, Rochester Institute of Technology, 84 Lomb Memorial Drive, Rochester, NY 14623, USA
[25] Institute for Theoretical Physics, Heidelberg University, Philosophenweg 12, D-69120, Heidelberg, Germany
[26] Max-Planck-Institut für Astronomie, Königstuhl 17, 69117 Heidelberg, Germany
[27] Steward Observatory, University of Arizona, 933 N Cherry Avenue, Tucson, AZ 85721, USA
[28] Department of Astronomy, School of Physics, Peking University, Beijing 100871, People's Republic of China
[29] Institute of Cosmology and Gravitation, University of Portsmouth, Dennis Sciama Building, Burnaby Road, Portsmouth, PO1 3FX, UK
[30] Centre for Astrophysics Research, University of Hertfordshire, Hatfield, AL10 9AB, UK
[31] David A. Dunlap Department of Astronomy and Astrophysics, University of Toronto, 50 St. George Street, Toronto, Ontario, M5S 3H4, Canada
[32] Dunlap Institute for Astronomy and Astrophysics, 50 St. George Street, Toronto, Ontario, M5S 3H4, Canada
[33] Department of Astronomy, Tsinghua University, Beijing 100084, People's Republic of China
[34] Chinese Academy of Sciences South America Center for Astronomy (CASSACA), National Astronomical Observatories of China (NAOC), CAS, 20A Datun Road, Beijing 100012, People's Republic of China
[35] School of Astronomy and Space Sciences, University of Chinese Academy of Sciences, Beijing 100049, People's Republic of China
[36] NASA-Goddard Space Flight Center, Code 662, Greenbelt, MD 20771, USA
[37] Center for Computational Astrophysics, Flatiron Institute, 162 5th Avenue, New York, NY 10010, USA
[38] University of Massachusetts Amherst, 710 North Pleasant Street, Amherst, MA 01003-9305, USA
[39] DTU Space, Technical University of Denmark, Elektrovej 327 DK2800 Kgs. Lyngby, Denmark
[40] Instituto de Alta Investigación, Universidad de Tarapacá, Casilla 7D, Arica, Chile
[41] Instituto de Estudios Astrofícos, Facultad de Ingeniería y Ciencias, Universidad Diego Portales, Av. Ejército 441, Santiago, Chile
[42] Millenium Nucleus for Galaxies (MINGAL), Chile
[43] Department of Computer Science, Aalto University, P.O. Box 15400, FI-00076 Espoo, Finland
[44] Department of Physics, University of Helsinki, P.O. Box 64, FI-00014 Helsinki, Finland
[45] Department of Physics and Astronomy, University of California, Riverside, 900 University Avenue, Riverside, CA 92521, USA
[46] Department of Physics, Graduate School of Science, The University of Tokyo, 7-3-1 Hongo, Bunkyo, Tokyo 113-0033, Japan
[47] Department of Pure and Applied Physics, Graduate School of Advanced Science and Engineering, Faculty of Science and Engineering, Waseda University, 3-4-1, Okubo, Shinjuku, Tokyo, 169-8555, Japan

[48] Waseda Research Institute for Science and Engineering, Faculty of Science and Engineering, Waseda University, 3-4-1, Okubo, Shinjuku, Tokyo, 169-8555, Japan
[49] Department of Astronomy, University of Michigan, 1085 S. University Avenue, Ann Arbor, MI 48109, USA
[50] National Astronomical Observatory of Japan, 2-21-1 Osawa, Mitaka, Tokyo, 181-8588, Japan
[51] School of Physics and Technology, Wuhan University, Wuhan 430072, People's Republic of China
[52] Department of Astronomy, University of Illinois at Urbana-Champaign, Urbana, IL 61801, USA
[53] Niels Bohr Institute, University of Copenhagen, Jagtvej 128, DK-2200, Copenhagen N, Denmark
[54] Jet Propulsion Laboratory, California Institute of Technology, 4800 Oak Grove Drive, Pasadena, CA 91001, USA
[55] Chinese Academy of Sciences South America Center for Astronomy, National Astronomical Observatories, CAS, Beijing 100101, People's Republic of China
[56] Departamento de Astronomía, Universidad de Chile, Casilla 36-D, Santiago, Chile
[57] Aix Marseille Univ, CNRS, CNES, LAM, Marseille, France
[58] Research School of Astronomy and Astrophysics, Australian National University, Cotter Road, Weston Creek, ACT 2611, Australia
[59] ARC Centre of Excellence for All Sky Astrophysics in 3 Dimensions (ASTRO 3D), Australia
[60] Department of Physics and Astronomy, University of Kentucky, 505 Rose Street, Lexington, KY 40506, USA
[61] Department of Astronomy, The University of Washington, Seattle, WA 98195, USA
[62] Institute for Astronomy, University of Hawai'i at Manoa, 2680 Woodlawn Drive, Honolulu, HI 96822, USA

Abstract

JWST has revealed a new high-redshift population called little red dots (LRDs). Since LRDs may be in the early phase of black hole growth, identifying them in the early Universe is crucial for understanding the formation of the first supermassive black holes. However, no robust LRD candidates have been identified at $z > 10$, because commonly used NIRCam photometry covers wavelengths up to $\sim 5\,\mu m$ and is insufficient to capture the characteristic V-shaped spectral energy distributions (SEDs) of LRDs. In this study, we present the first search for $z \gtrsim 10$ LRD candidates using both NIRCam and MIRI imaging from COSMOS-Web, which provides the largest joint NIRCam-MIRI coverage to date ($0.20\,\mathrm{deg}^2$). Taking advantage of MIRI/F770W to remove contaminants, we identify one robust candidate, CW-LRD-z10 at $z_{\mathrm{phot}} = 10.5^{+0.7}_{-0.6}$ with $M_{\mathrm{UV}} = -19.9^{+0.1}_{-0.2}$ mag. CW-LRD-z10 exhibits a compact morphology, a distinct V-shaped SED, and a nondetection in F115W, all consistent with being an LRD at $z \sim 10$. Based on this discovery, we place the first constraint on the number density of LRDs at $z \sim 10$ with $M_{\mathrm{UV}} \sim -20$ of $1.2^{+2.7}_{-1.0} \times 10^{-6}\,\mathrm{Mpc}^{-3}\,\mathrm{mag}^{-1}$, suggesting that the fraction of LRDs among the overall galaxy population increases with redshift, reaching $\sim 3\%$ at $z \sim 10$. Although deep spectroscopy is necessary to confirm the redshift and the nature of CW-LRD-z10, our results imply that LRDs may be a common population at $z > 10$, playing a key role in the first supermassive black hole formation.

Unified Astronomy Thesaurus concepts: Active galactic nuclei (16); Galaxy evolution (594); High-redshift galaxies (734); Galaxy formation (595)

1. Introduction

The James Webb Space Telescope (JWST; J. Rigby et al. 2023) has revolutionized the study of high-redshift active galactic nuclei (AGNs). Despite its limited field of view, JWST's deep imaging has led to the discovery of numerous AGNs with the UV absolute magnitude of $M_{\mathrm{UV}} \gtrsim -22$,[63] fainter than typical UV luminous quasars with $M_{\mathrm{UV}} \lesssim -24$, even at $z \gtrsim 4$ (e.g., Y. Harikane et al. 2023a; D. D. Kocevski et al. 2023; M. Onoue et al. 2023; R. Maiolino et al. 2024a; J. Scholtz et al. 2025; A. J. Taylor et al. 2025a). Assuming a single-epoch virial mass estimator (e.g., A. Laor 1998; M. Vestergaard & B. M. Peterson 2006; Y. Shen 2013) with broad lines, these AGNs are found to host supermassive black holes (SMBHs) with black hole masses of $M_{\mathrm{BH}} \gtrsim 10^6 M_\odot$, reaching to ~ 3 dex lower than the masses of the most luminous quasars at similar epochs (e.g., X. Fan et al. 2001; C. J. Willott et al. 2010; Y. Shen et al. 2011; F. Wang et al. 2021; E. Bañados et al. 2023; J. Yang et al. 2023). Recent studies have reported that the luminosity function of these JWST-found AGNs at the high-z Universe (e.g., H. B. Akins

et al. 2024; V. Kokorev et al. 2024a; D. D. Kocevski et al. 2025; X. Lin et al. 2025a) is 1–2 dex higher than the extrapolation of the luminosity function of UV luminous quasars based on the ground-based surveys (Y. Matsuoka et al. 2016; M. Akiyama et al. 2018; M. Niida et al. 2020; X. Shen et al. 2020), suggesting the rapid formation of an abundant SMBH population in the early Universe.

In particular, a previously unseen population that is likely associated with SMBHs has emerged, namely little red dots (LRDs), from early JWST observations (e.g., H. B. Akins et al. 2023, 2024; D. D. Kocevski et al. 2023; I. Labbé et al. 2023; G. Barro et al. 2024a; L. J. Furtak et al. 2024; J. E. Greene et al. 2024; J. Matthee et al. 2024; D. J. Setton et al. 2024; K. N. Hainline et al. 2025; R. E. Hviding et al. 2025). LRDs are characterized by their compact morphology in the rest-optical wavelength, with the strongest constraint of $r_e \lesssim 30$ pc provided by L. J. Furtak et al. (2024) through strong gravitational lensing. LRDs also exhibit unique V-shaped spectral energy distributions (SEDs), which consist of a rest-optical steep red continuum and a rest-UV excess (e.g., H. B. Akins et al. 2023, 2024; D. D. Kocevski et al. 2023; I. Labbé et al. 2023; G. Barro et al. 2024a; L. J. Furtak et al. 2024; J. Matthee et al. 2024) with a pronounced slope change around the Balmer limit (e.g., D. J. Setton et al. 2024), often with a Balmer break (e.g., V. Kokorev et al. 2024b; I. Labbe et al. 2024; A. de Graaff et al. 2025; R. P. Naidu et al. 2025a; B. Wang et al. 2025). Spectroscopic observations have found broad ($>1000\,\mathrm{km\,s}^{-1}$) hydrogen Balmer emission lines in

---

[63] In this study, we define M_{UV} as the absolute magnitude in rest-frame 1450 Å, following the definition in D. D. Kocevski et al. (2025).

photometrically selected LRD candidates. Assuming these broad lines are attributed to type-I AGNs and applying the single-epoch virial mass estimator (e.g., A. Laor 1998; M. Vestergaard & B. M. Peterson 2006; Y. Shen 2013), previous studies have estimated their black hole masses as $M_{\rm BH} \gtrsim 10^6 M_\odot$ (e.g., L. J. Furtak et al. 2024; J. E. Greene et al. 2024; J. Matthee et al. 2024; I. Labbe et al. 2025).

Unlike typical low-redshift AGNs, LRDs remain undetected in X-rays (H. B. Akins et al. 2024; T. T. Ananna et al. 2024; M. Yue et al. 2024; X. Lin et al. 2025b; R. Maiolino et al. 2025) and radio (H. B. Akins et al. 2024; G. Mazzolari et al. 2024; X. Lin et al. 2025b; K. Perger et al. 2025), even with stacking analyses. While we cannot detect a significant variability in broadband photometry for most cases (M. Kokubo & Y. Harikane 2024; W. L. Tee et al. 2025; Z. Zhang et al. 2025a; S. Zhou et al. 2025), some studies have reported significant detection of variability in the Hα equivalent width (EW) thanks to longer time baselines due to gravitational lensing (L. J. Furtak et al. 2025; X. Ji et al. 2025a). These nondetections of typical AGN-like features may suggest a non-AGN nature. An explanation of LRDs not related to SMBHs is that they are massive, compact galaxies (e.g., H. B. Akins et al. 2023, 2024; I. Labbé et al. 2023). However, this scenario implies large stellar masses, which may exceed the number densities of such massive halos predicted by the ΛCDM model (M. Boylan-Kolchin 2023), and the densest stellar system discovered so far (J. F. W. Baggen et al. 2024; I. Labbe et al. 2024; Y. Ma et al. 2025a). On the other hand, it has also been proposed that super-Eddington accretion could potentially explain the absence of X-ray and variability signatures in cases where LRDs are indeed AGNs (e.g., K. Inayoshi et al. 2024; E. Lambrides et al. 2024; P. Madau & F. Haardt 2024; F. Pacucci & R. Narayan 2024).

One of the surprising aspects of LRDs is their abundance. The number density of LRDs peaks at $z \sim 6$–8, corresponding to about 3% and 10% of the galaxy population with $M_{\rm UV} = -20$ and -22, respectively, at $z \sim 7$ (D. D. Kocevski et al. 2025). It has also been reported that LRDs are more abundant by $\sim$0.6 dex at $z \sim 5$ compared to X-ray AGNs (S. Parsa et al. 2018) and by $\sim$1 dex at $z \sim 7$ compared to color-selected AGNs (G. Kulkarni et al. 2019) with the same UV luminosity (D. D. Kocevski et al. 2025), suggesting that LRDs represent a crucial population for understanding BH evolution in the early Universe.

Typical photometric selection for LRD candidates is performed using their compactness and characteristic V-shape SEDs in JWST/NIRCam photometry. For instance, I. Labbé et al. (2023) and V. Kokorev et al. (2024a) used multiple color-selection criteria, while D. D. Kocevski et al. (2025) used SED slopes to identify V-shape profiles. Similarly, H. B. Akins et al. (2024) employed the single color threshold of $m_{\rm F277W} - m_{\rm F444W} > 1.5$ and compactness criterion to select LRD candidates.

Spectroscopic observations of these photometrically selected LRD candidates have detected broad Balmer emission lines, confirming their nature as LRDs (e.g., J. E. Greene et al. 2024). Spectroscopic surveys have confirmed that these photometrically selected LRD candidates are highly reliable, with low contamination rates ($\sim$90%). However, they also suggested a completeness of $\sim$50%, indicating that a part of the LRD population may have been missed in previous photometric selections (R. E. Hviding et al. 2025; X. Lin et al. 2025a). Among previously selected LRD

candidates, some studies (e.g., K. N. Hainline et al. 2025; Z. Zhang et al. 2025b) have reported contamination where a red continuum could not be spectroscopically confirmed, and the V-shaped SED seen in the photometry was instead caused by strong emission lines. However, the fraction of such contamination cases is estimated to be $\sim$20%–35% of LRD candidates, implying that the majority of candidates exhibit both a red continuum and broad Balmer emission lines in their spectrum.

Based on the redshift distribution from D. D. Kocevski et al. (2025), K. Inayoshi (2025) reported that the number density of LRDs with $M_{\rm UV} < -18$ follows a log-normal distribution as a function of cosmic time, suggesting that LRDs may be driven by stochastic phenomena. With LRDs seemingly being a distinct population with unique characteristics in the early Universe, one hypothesis is that they may represent the first or second accretion episodes following the formation of their seed black holes, potentially undergoing rapid growth via super-Eddington accretion (K. Inayoshi 2025). To test the evolution of such an LRD population observationally, we need to constrain the LRD population over a wide redshift range. Efforts to identify LRDs at lower redshifts ($z < 4$; e.g., R. Lin et al. 2025) are not limited to JWST observations (D. D. Kocevski et al. 2025; M.-Y. Zhuang et al. 2025), but have also been extended to wider-area surveys using Euclid (Euclid Collaboration et al. 2025) and Subaru's Hyper Suprime-Cam (HSC) imaging (Y. Ma et al. 2025b), combined with archival infrared survey data. Recently, X. Lin et al. (2025b) and X. Ji et al. (2025a) identified LRD analogs even at $z \sim 0.1$–0.2, based on spectroscopically confirmed objects from the Sloan Digital Sky Survey. Their results are consistent with a decline from $z \sim 5$–6 or indicate a higher number density than predicted by K. Inayoshi (2025); however, there is still a possibility of contamination since sources lack spectroscopic confirmation.

Expanding LRD searches not only toward lower redshift but also to higher redshift is crucial for constraining the evolution of the LRD population itself, as well as for probing the first SMBHs in the Universe. Currently, three spectroscopically confirmed AGNs (not LRDs) have been reported at $z_{\rm spec} > 10$: GHZ-9 ($z_{\rm spec} = 10.145 \pm 0.010$; O. E. Kovács et al. 2024; L. Napolitano et al. 2025), UHZ-1 ($z_{\rm spec} = 10.073 \pm 0.002$; A. D. Goulding et al. 2023; Á. Bogdán et al. 2024), and GN-z11 ($z_{\rm spec} = 10.6034 \pm 0.0013$; P. A. Oesch et al. 2016; L. Jiang et al. 2021; A. J. Bunker et al. 2023; R. Maiolino et al. 2024b; J. Scholtz et al. 2024). On the other hand, the current highest spectroscopic redshift for an LRD is CAPERS-LRD-z9 at $z_{\rm spec} = 9.288$ (A. J. Taylor et al. 2025b), which was selected through photometry (H. B. Akins et al. 2024; G. Barro et al. 2024b; D. D. Kocevski et al. 2025).

A previous study (D. D. Kocevski et al. 2025) selected 13 LRD candidates at $z_{\rm photo} \gtrsim 10$ solely from NIRCam photometry. Among these, six objects have been spectroscopically observed; however, no clear LRDs have been confirmed at $z \gtrsim 10$ (see Appendix A for each case). As suggested in D. D. Kocevski et al. (2025) and K. N. Hainline et al. (2025), this demonstrates that selecting $z \sim 10$ LRDs solely with NIRCam is inherently challenging. Since F444W, the longest-wavelength filter in NIRCam, is too close to the Balmer limit at $z \sim 10$ ($\sim$4 μm), it is difficult to separate the contribution of emission lines or a stellar-origin Balmer break from the characteristic red slope of LRDs. With MIRI photometry at longer wavelengths, it becomes possible to remove such contamination and select
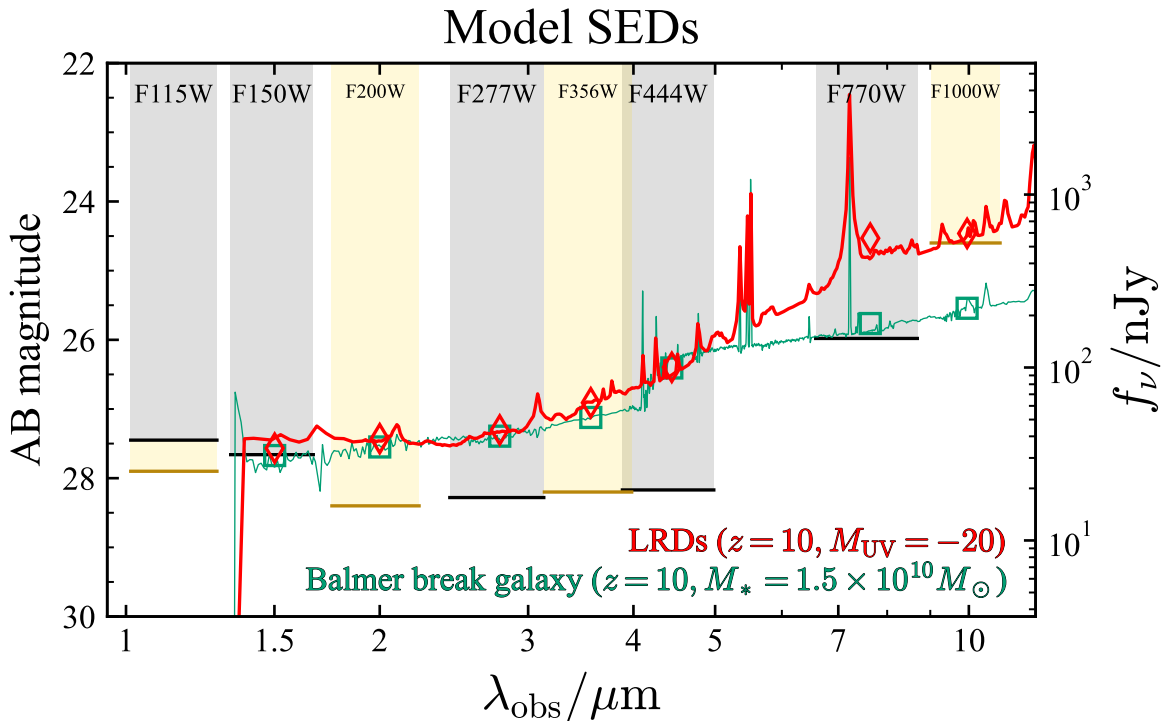
Figure 1. Model spectral energy distribution (SED) of a $z = 10$ LRD with $M_{UV} = -20$ (red) and 5σ depth for point sources in COSMOS-Web (F115W, F150W, F277W, F444W, and F770W) from C. M. Casey et al. (2023) and in COSMOS-3D (F115W, F200W, F356W, and F1000W) shown in gray and gold rectangles, respectively. Model SEDs of potential contaminants of the $z \sim 10$ LRD photometric selection, a $z = 10$ galaxy with a stellar-origin Balmer break with $A_V = 0.5$ and $M_* = 1.5 \times 10^{10} M_\odot$, are overlaid. The LRD model SED is from H. B. Akins et al. (2024), and the galaxy SED is generated using FSPS (C. Conroy et al. 2009; C. Conroy & J. E. Gunn 2010). The predicted model photometry is shown with diamonds for the LRD and squares for the galaxy. MIRI photometry is essential to distinguish between $z \sim 10$ LRDs and $z \sim 10$ galaxies with stellar-origin Balmer break.

$z \gtrsim 10$ LRDs more reliably. In this context, P. G. Pérez-González et al. (2024) reported an NIRCam dark galaxy detected in MIRI/F1000W. While they discussed the possibility that this object is an LRD at $z \sim 14$, it is fainter than 30–30.5 mag in the NIRCam wavelength range and lacks spectroscopic confirmation; thus, its true nature remains uncertain. Based on the log-normal distribution proposed by K. Inayoshi (2025), the number density of LRDs declines toward higher redshifts from $z \sim 6$. Thus, to robustly identify $z \sim 10$ LRDs, a large survey volume with joint NIRCam and MIRI coverage is essential.

In this study, we utilize data from COSMOS-Web, which provides the largest combined NIRCam and MIRI survey area to date ($\sim 0.18 \, \text{deg}^2$), to search for $z \sim 10$ LRDs and for the first time to place constraints on their luminosity function. In Section 2 we describe the data, and in Sections 3 and 4, we present the selection methods and the follow-up analysis of a selected candidate. Section 5 shows the results of the follow-up analysis of the candidate. Then, in Section 6, we constrain the luminosity function of LRDs at $z \sim 10$ and discuss their implications. Throughout this paper, we use the AB magnitude system (J. B. Oke & J. E. Gunn 1983) and assume a standard cosmology with $H_0 = 70 \, \text{km s}^{-1} \text{Mpc}^{-1}$, $\Omega_m = 0.30$, and $\Omega_\Lambda = 0.70$.

2. Data

2.1. Survey Field

As discussed above, we require data from a wide-area survey that combines JWST/NIRCam (M. J. Rieke et al. 2023) and MIRI (P. Bouchet et al. 2015) imaging to robustly search

for $z \sim 10$ LRDs. Therefore, we use COSMOS-Web (GO 1727,[64] PI: J. Kartaltepe and C. Casey; C. M. Casey et al. 2023), a JWST Cycle 1 Treasury Program with the largest NIRCam and MIRI coverage to date. COSMOS-Web covers $0.54 \, \text{deg}^2$ with NIRCam using four filters: F115W, F150W, F277W, and F444W. Simultaneously, COSMOS-Web covers $0.20 \, \text{deg}^2$ with MIRI F770W. The overlapping area between the NIRCam and MIRI coverage is $0.18 \, \text{deg}^2$, which is the effective field for our LRD search utilizing both NIRCam and MIRI photometry. Figure 1 illustrates the depth of COSMOS-Web observations with a stacked model SED of photometrically selected LRDs provided in H. B. Akins et al. (2024),[65] assuming $z = 10$ and $M_{UV} = -20$ (red line). To separate LRDs from other lower-z dusty sources based on the presence of a UV excess with F150W and F277W, we focus only on sources brighter than $M_{UV} \lesssim -19.5$ mag, which can be detected in both F150W and F277W with a $\gtrsim 3\sigma$ significance.

The COSMOS-Web field is also partially covered by COSMOS-3D (GO 5893,[66] PI: K. Kakiichi), which includes NIRCam imaging in F115W, F200W, and F356W. Observations are ongoing, and COSMOS-3D will cover a part of the full COSMOS-Web field: $\sim 0.33 \, \text{deg}^2$ ($\sim 0.14 \, \text{deg}^2$) with NIRCam (MIRI). To uniformly select $z \sim 10$ LRDs across the wider field, the color selection in this study only utilizes photometry from COSMOS-Web.

2.2. Imaging Data

The candidate selection process (Section 3) utilizes the catalog photometry from COSMOS2025 (M. Shuntov et al. 2025, Section 2.3): JWST/NIRCam (F115W, F150W, F277W, and F444W) and JWST/MIRI (F770W) from COSMOS-Web combined with Subaru/HSC (*ugriz*) and the Hubble Space Telescope (HST) Advanced Camera for Surveys (ACS; F814W). For the subsequent follow-up analysis of the selected candidate (Section 4), we utilize all available imaging data, including JWST/NIRCam (F115W, F200W, and F356W) and JWST/MIRI (F1000W and F2100W) from COSMOS-3D and HST/ACS (F606W).

2.2.1. JWST/NIRCam

We reduce all available NIRCam imaging data through a custom pipeline, as described in M. Franco et al. (2025a; see H. B. Akins et al. 2025, in preparation for details). The raw NIRCam images are processed through the JWST Calibration Pipeline version 1.17.1 (H. Bushouse et al. 2025), with the addition of several custom modifications, including the subtraction of $1/f$ noise and sky background. We use the Calibration Reference Data System (CRDS)[67] pmap 1331. The $1/f$ noise is subtracted through the iterative source masking and amp-row median subtraction as described in M. B. Bagley et al. (2023), and wisps—scattered light features present in several NIRCam short wavelength (SW) detectors—are removed by rescaling and subtracting the version 3 templates provided by STScI.[68] Background subtraction is performed using the iterative source masking procedure described in M. B. Bagley et al. (2023). Astrometric calibration is conducted via the JWST/HST alignment tool (JHAT; A. Rest et al. 2023), with a reference catalog based on an HST/F814W $0\farcs03$ pixel^{-1} mosaic of the field (A. M. Koekemoer et al. 2007) with astrometry tied to Gaia-DR3 (Gaia Collaboration et al. 2023). All NIRCam mosaics are resampled to a uniform pixel scale of $0\farcs03$ pixel^{-1}. The 5σ point-source limiting magnitude for COSMOS-Web NIRCam images is summarized in M. Franco et al. (2025a), and those for COSMOS-3D images are 28.4 and 28.2 in F200W and F356W, respectively. Note that F115W has been processed by combining both the COSMOS-Web and COSMOS-3D data, resulting in a point-source limiting magnitude of 27.9.

2.2.2. JWST/MIRI

For MIRI imaging, we use F1000W and F2100W imaging from COSMOS-3D with COSMOS-Web's F770W, thereby extending our MIRI wavelength coverage up to ∼25 μm. The F770W data reduction of COSMOS-Web is presented in S. Harish et al. (2025), with key steps briefly summarized below. The F770W data were reduced using the JWST Calibration Pipeline version 1.12.5 (H. Bushouse et al. 2023) with JWST Calibration Reference Data System Pipeline Context version 1130. The reduction includes the standard rate calculation, jump detection, slope fitting, nonlinearity correction, flat-fielding, and flux scale conversion, as well as a highly customized master background subtraction (see S. Harish et al. 2025 for the demonstration of quality improvement). The astrometry correction is also highly customized with source extraction and aligning using SExtractor and JWST pipeline's `tweakreg` module, and with the same absolute reference catalog as for NIRCam reduction. The Lyot detector area was also processed together with the main imager area to increase the field of view, which provides a good quality of data after applying our customized master background subtraction. F770W image is also resampled to a pixel scale of $0\farcs03$ pixel^{-1}. The F1000W and F2100W data were reduced using the JWST Calibration Pipeline version 1.12.5 (H. Bushouse et al. 2023) with JWST Calibration Reference Data System Pipeline Context version 1303. F1000W and F2100W images are resampled to a pixel scale of $0\farcs11$ pixel^{-1}.

2.2.3. HST/ACS

For the HST data, we make use of the ACS F814W mosaics (A. M. Koekemoer et al. 2007), which have been reprocessed with up-to-date calibration reference files and aligned to Gaia-DR3 (Gaia Collaboration et al. 2023), serving as the astrometric reference frame for all of the above JWST data. We also make use of the ACS F606W mosaics, which are a full-depth combination of data from CANDELS (N. A. Grogin et al. 2011; A. M. Koekemoer et al. 2011) and CLUTCH (HST program ID 17802, PI: J. Kartaltepe), also aligned to the HST ACS F814W astrometric grid. These HST mosaics have been resampled to a uniform pixel scale of $0\farcs03$ pixel^{-1}.

2.3. Photometric Catalog

We select LRD candidates using photometry from the COSMOS2025 catalog (M. Shuntov et al. 2025), which provides a comprehensive photometric dataset for the COSMOS-Web field containing 37 bands covering 0.3–8 μm from Subaru/HSC to JWST/MIRI (not including COSMOS-3D photometry). Among them, we use the information from Subaru/HSC (*g*, *r*, *i*, *z*, and *y*), HST/ACS (F814W), JWST/NIRCam (F115W, F150W, F277W, F444W), and JWST/MIRI (F770W) in the selection process (Section 3.2). Note that we use the photometry from COSMOS2025 only for the photometric selection described in Section 3.2. After the selection, we remeasure the photometry (Section 4.1) based on the imaging data described in Section 2.2 to apply a consistent method across all available bands, including filters not covered in the COSMOS2025 catalog.

2.4. Grism Data

COSMOS-3D also performs a Wide Field Slitless Spectroscopy (WFSS) survey with NIRCam/F444W, covering a part of the COSMOS-Web field. This WFSS observation has covered the selected candidate described later. The COSMOS-3D grism data is processed with two different processing software, `unfold_jwst` (F. Wang et al. 2023) and `Grizli`[69] (G. Brammer 2023a), to reduce the software dependencies and obtain robust results (see K. Kakiichi 2025, in preparation for detailed data processing).
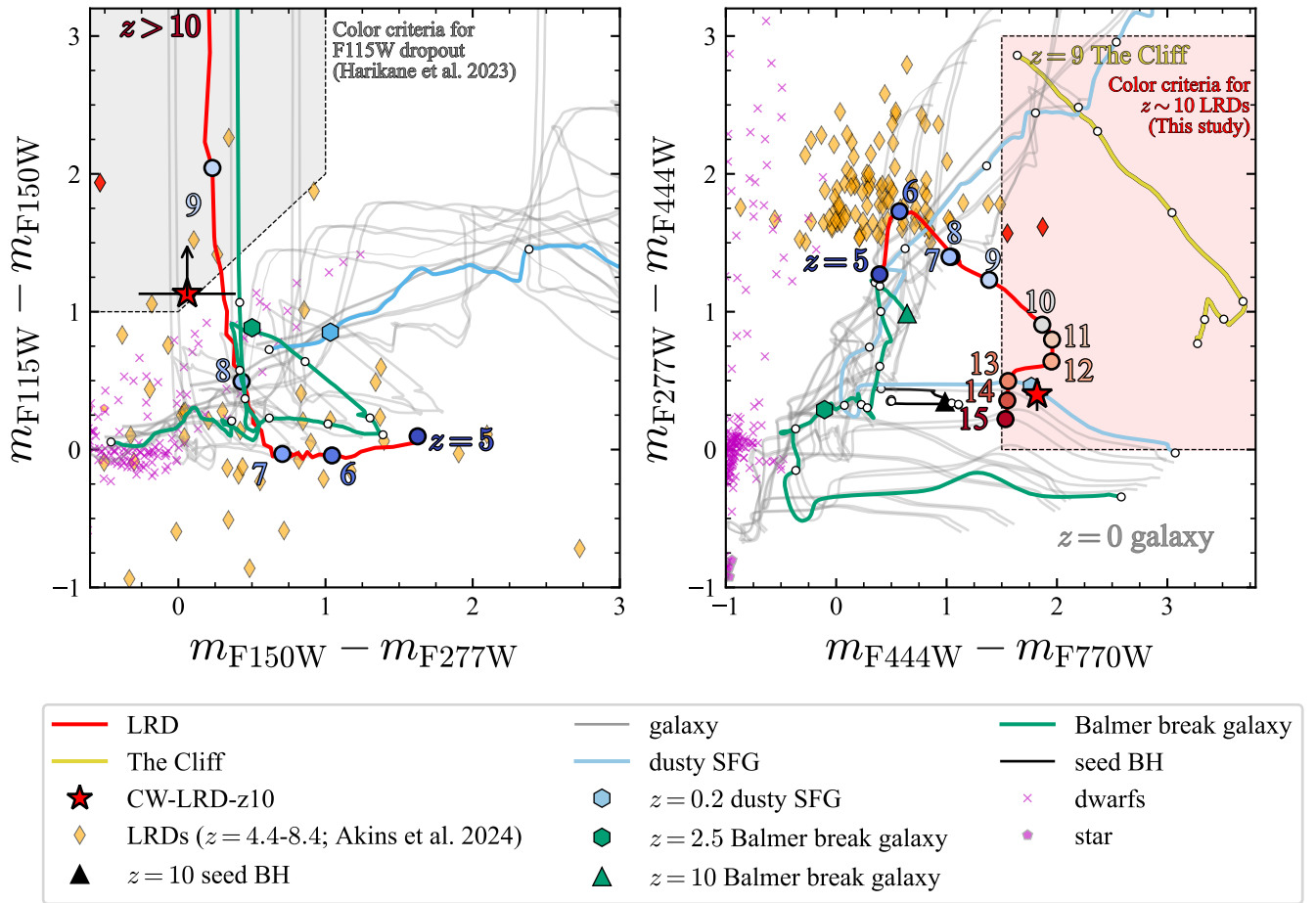
The candidate has also been covered in the NIRCam/F322W2 WFSS observation in POPPIES (GO 5398,[70] PI: J. Kartaltepe and M. Rafelski). However, CW-LRD-z10

---

[67] jwst-crds.stsci.edu
[68] https://stsci.app.box.com/s/1bymvf1lkrqbdn9rnkluzqk30e8o2bne
[69] https://github.com/gbrammer/grizli
[70] www.stsci.edu/jwst-program-info/program/?program=5398

Figure 2. Color–color diagrams based on the LRD model SEDs from H. B. Akins et al. (2024; red lines). The left and right panels show $m_{F115W} - m_{F150W}$ versus $m_{F150W} - m_{F277W}$ and $m_{F277W} - m_{F444W}$ versus $m_{F444W} - m_{F770W}$, respectively. The red filled region defined by $0 < m_{F277W} - m_{F444W} < 2.25$ and $1.5 < m_{F444W} - m_{F770W}$ can effectively distinguish $z \sim 10$ LRDs from other objects. The selected candidate in this study, CW-LRD-z10, is highlighted with a red star with error bars. Note that $m_{F115W} - m_{F150W}$ color for CW-LRD-z10 is a 2σ lower limit. CW-LRD-z10 also passes the color criteria for F115W dropouts (Y. Harikane et al. 2023b) shown by the gray shaded region in the left panel. Model galaxy SEDs generated using FSPS (C. Conroy et al. 2009; C. Conroy & J. E. Gunn 2010) with various star formation histories and dust attenuation values at $z = 0$–10 are shown in gray solid lines. Of these, we highlight two cases: (1) a stellar-origin Balmer break (with an f_ν ratio of ∼2) and $A_V = 0.5$ (green), and (2) a dusty star-forming galaxy (SFG) model with $A_V = 5$ (cyan). Seed BH models from K. Inayoshi et al. (2022) at $z = 8$–14 and LRDs with an extremely strong Balmer break at $z = 9$–15, assuming the spectrum of The Cliff in A. de Graaff et al. (2025), are shown in black and orange, respectively. For these model SEDs, dots are placed at redshift intervals of $\Delta z = 1$. Specifically, $z = 10$ Balmer break galaxy, $z = 10$ seed BH, $z = 2.5$ galaxy with stellar-origin Balmer break, and $z = 0.2$ dusty SFG are shown in green triangle, black triangle, green hexagon, and cyan hexagon, respectively. Photometrically selected LRDs from H. B. Akins et al. (2024) with a signal-to-noise ratio (S/N) > 3 are shown as orange diamonds; among them are two objects that pass our color selection (red diamonds). Dwarf stars and main-sequence stars from the BT-Settl model (F. Allard et al. 2012) are plotted in magenta crosses and pentagons, respectively.

lies near the edge of the WFSS field of view, and a usable spectrum could not be obtained in POPPIES.

3. Sample Selection

3.1. Evolution on the Color–Color Diagram

To define robust color thresholds for selecting $z \sim 10$ LRDs, we model their redshift evolution on a color–color diagram. The thick red line in Figure 2 illustrates the redshift evolution of LRDs on the $m_{F115W} - m_{F150W}$ versus $m_{F150W} - m_{F277W}$ and the $m_{F277W} - m_{F444W}$ versus $m_{F444W} - m_{F770W}$ planes. Here, we assume the model SED for stacked LRDs from H. B. Akins et al. (2024), evolved from $z \sim 5$ to 15.

We also plot the color evolution of LRDs with a strong Balmer break by using the NIRSpec/PRISM spectrum of such an LRD at $z = 3.548$, "The Cliff" (A. de Graaff et al. 2025), obtained in GO 4233[71] (RUBIES, PI: A. de Graaff and

G. Brammer). We download the spectrum from the Dawn JWST archive,[72] which was processed with msaexp (G. Brammer 2023b; A. de Graaff et al. 2024; K. E. Heintz et al. 2024), a tool for extracting spectra directly from the telescope exposures. We further perform flux calibration to correct for possible slit loss by adopting a second-order polynomial function to match the spectrum with the NIRCam photometry (F090W, F115W, F150W, F200W, F277W, F356W, F444W), taken from the Dawn JWST Archive (DJA) morphological catalogs based on SExtractor++ (E. Bertin et al. 2020; M. Kümmel et al. 2020). The correction factor ranges from 0.96–1.08, indicating that the DJA spectrum and photometry for The Cliff are basically consistent with each other (differences are <0.1 mag). Note that The Cliff is not plotted in Figure 2 (left panel) because we cannot estimate its F115W and F150W photometry at these redshifts due to the limited wavelength coverage of the spectral data ($\lambda_{rest} \gtrsim 0.14\,\mu m$). The stacked LRD

SED (H. B. Akins et al. 2024) has a rest-frame Hα EW of $\sim$700 Å (including both broad and narrow components) and the rest-frame optical continuum slope, measured in $0.38 < \lambda_{\rm rest}/\mu$m < 0.8 after masking Hβ+[O III] and Hα lines, of $\beta \sim 0.4$ ($f_\lambda \propto \lambda^\beta$). The Cliff has a lower rest-frame Hα EW of $\sim$400 Å and a similar optical continuum slope of $\beta \sim 0.3$. Thus, The Cliff has an Hα contribution and an optical slope similar to the stacked model SED (though slightly weaker Hα), with the main difference being its much stronger Balmer break.

To assess the possibility of contamination, in Figure 2, we also plot the color evolution of the predicted SED of seed BHs that assumes a super-Eddington accreting SMBHs with $M_{\rm BH} \sim 10^6 M_\odot$ (K. Inayoshi et al. 2022; $z = 8$–14, black line) and Galactic stars (main-sequence and dwarfs assuming $T_{\rm eff} = 400$–4000 K) from the BT-Settl model with solar metallicity (F. Allard et al. 2012; magenta pentagon and cross, respectively). Additionally, we generate galaxy SED models using Flexible Stellar Population Synthesis (FSPS; C. Conroy et al. 2009; C. Conroy & J. E. Gunn 2010), assuming a delayed-τ star formation history with $t_{\rm age} = 11.3$ Gyr, which is 0.95 times of the Hubble time at $z = 0.2$, $\tau = 0.01$, 0.1, 1, and 10 Gyr, and dust attenuation with $A_V = 0$, 0.5, 1, 3, and 5 mag. These galaxy SED models include nebular emission lines (N. Byler et al. 2017) based on Cloudy (G. J. Ferland et al. 1998, 2017). We fix the gas ionization parameter to $\log U = -2$ and gas metallicity to $\log (Z_{\rm gas}/Z_\odot) = -1$. We indicate the color evolution of the synthetic galaxies at $z = 0$–10 (gray lines).

From Figure 2 (left panel), we see that LRDs have a high value for the $m_{\rm F115W} - m_{\rm F150W}$ color due to the Lyman break entering F115W, a feature similar to galaxies at $z > 8$. However, the $m_{\rm F150W} - m_{\rm F277W}$ color also overlaps significantly with other galaxy populations. Therefore, the $m_{\rm F115W} - m_{\rm F150W}$ and $m_{\rm F150W} - m_{\rm F277W}$ colors are insufficient to distinguish $z \sim 10$ LRDs from normal $z \sim 10$ galaxies, while being effective at identifying dropouts, as shown by the color criteria for F115W-dropout galaxies (gray-filled region, from Y. Harikane et al. 2023b).

From Figure 2 (right panel), LRDs have $m_{\rm F277W} - m_{\rm F444W} > 1.5$ at $z \sim 6$, which is the selection threshold for LRDs in H. B. Akins et al. (2024). Toward higher redshift, the Balmer limit shifts closer to F444W, i.e., F277W traces the flat rest-UV part of the spectrum, and Hα and [OIII]+Hβ move out of the F444W coverage. As a result, the $m_{\rm F277W} - m_{\rm F444W}$ color decreases to $\sim$1.0 at $z \sim 10$. Thus, the $m_{\rm F277W} - m_{\rm F444W} > 1.5$ color cut used in H. B. Akins et al. (2024) is not effective for $z \sim 10$ LRDs. Because the Balmer limit shifts to $\sim 4\,\mu$m, and Hα falls into F770W at $z \sim 10$, the $m_{\rm F444W} - m_{\rm F770W}$ color increases, reaching $m_{\rm F444W} - m_{\rm F770W} \sim 2$ at $z \sim 10$. We also note that The Cliff exhibits a larger color, driven by its stronger Balmer break compared to stellar-origin Balmer breaks.

As shown, the color space, $m_{\rm F277W} - m_{\rm F444W}$ versus $m_{\rm F444W} - m_{\rm F770W}$, effectively isolates $z \sim 10$ LRDs from other sources. Seed BHs, showing strong Hα with rest-frame EW of $\sim$1000 Å, have $m_{\rm F444W} - m_{\rm F770W} < 1.5$ due to the absence of a red continuum spectrum. Brown dwarfs and main-sequence stars exhibit $m_{\rm F444W} - m_{\rm F770W} \lesssim 0$, far from $z \sim 10$ LRDs. Most normal galaxies are also well separated from $z \sim 10$ LRDs, though dusty star-forming galaxies (SFGs) at $z \sim 0.2$ could mimic LRD-like $m_{\rm F277W} - m_{\rm F444W}$ and $m_{\rm F444W} - m_{\rm F770W}$ colors. At $z \sim 0.2$, polycyclic aromatic hydrocarbon (PAH) emission bands at the rest-frame 3.3 μm and 6.2 μm

Table 1
Number of Objects Selected in Each Procedure

Step	Selection	#
0	COSMOS2025	784,016
1	`warn_flag=0`	694,341
2	In MIRI coverage	236,127
3	S/N in HSC, HST, and JWST	259
4	colors	18
5	compact	6
6	visual inspection	1

enter F444W and F770W, respectively, boosting the observed fluxes in those bands. Thus, $z \sim 0.2$ dusty SFGs can also reproduce an apparent slope change around $\lambda_{\rm obs} \sim 3$–4 μm, resembling the photometric SED of $z \sim 10$ LRDs. In Section 5, we further discuss the possibility of interlopers based on their SEDs and morphology.

3.2. Selection Procedures

We perform color-based selection using the COSMOS2025 photometric catalog (Section 2.3). The number of objects at each step in the selection is summarized in Table 1. The COSMOS2025 catalog contains 784,016 objects, of which 694,631 have `warn_flag=0` (good objects), indicating that they are not hot pixels or artifacts, and there is no inconsistency between ground and space observations (see M. Shuntov et al. 2025 for detail). Among them, 236,127 objects are located in the area with MIRI coverage and constitute the parent sample used in this study.

First, we require a detection with a signal-to-noise ratio (S/N) > 5 in F150W, F277W, F444W, and F770W, while undetected (S/N < 2) in F814W and F115W using the `snr_{filter}` columns, which give S/N within $0''2$ diameter apertures. As shown in Figure 1, the shallowest photometry relative to $z \sim 10$ LRD's SED in our dataset, i.e., the bottleneck for identifying $z \sim 10$ LRDs, is F150W. Sources with S/N$_{\rm F150W} \sim 5$ in COSMOS2025 have the median F150W photometry of 27.7 mag, which corresponds to $M_{\rm UV} \sim -19.5$ at $z \sim 9$. Therefore, LRDs with $M_{\rm UV} \gtrsim -19.5$ are not detected in F150W and thus cannot be selected in our sample. To exclude low-redshift galaxies, we also apply additional nondetection (S/N < 2) criteria in all of the HSC g, r, i, z, and y bands (`flux_model_hsc-{filter}`, `flux_err-cal_model_hsc-{filter}` columns).

We adopt the following new color criteria:

$$m_{\rm F277W} - m_{\rm F444W} > 0, \tag{1}$$

$$m_{\rm F277W} - m_{\rm F444W} < 3.0, \tag{2}$$

$$m_{\rm F444W} - m_{\rm F770W} > 1.5, \tag{3}$$

as shown in the red filled region in the color–color diagram shown in the right panel of Figure 2. Magnitudes are from the columns `mag_auto_{filter}`, measured in small elliptical apertures with corrections for the Kron aperture and point-spread function (PSF) differences. Note that this color selection is capable of identifying $z \gtrsim 9$ LRDs even in cases where they exhibit an extremely strong Balmer break, such as seen in The Cliff (A. de Graaff et al. 2025).
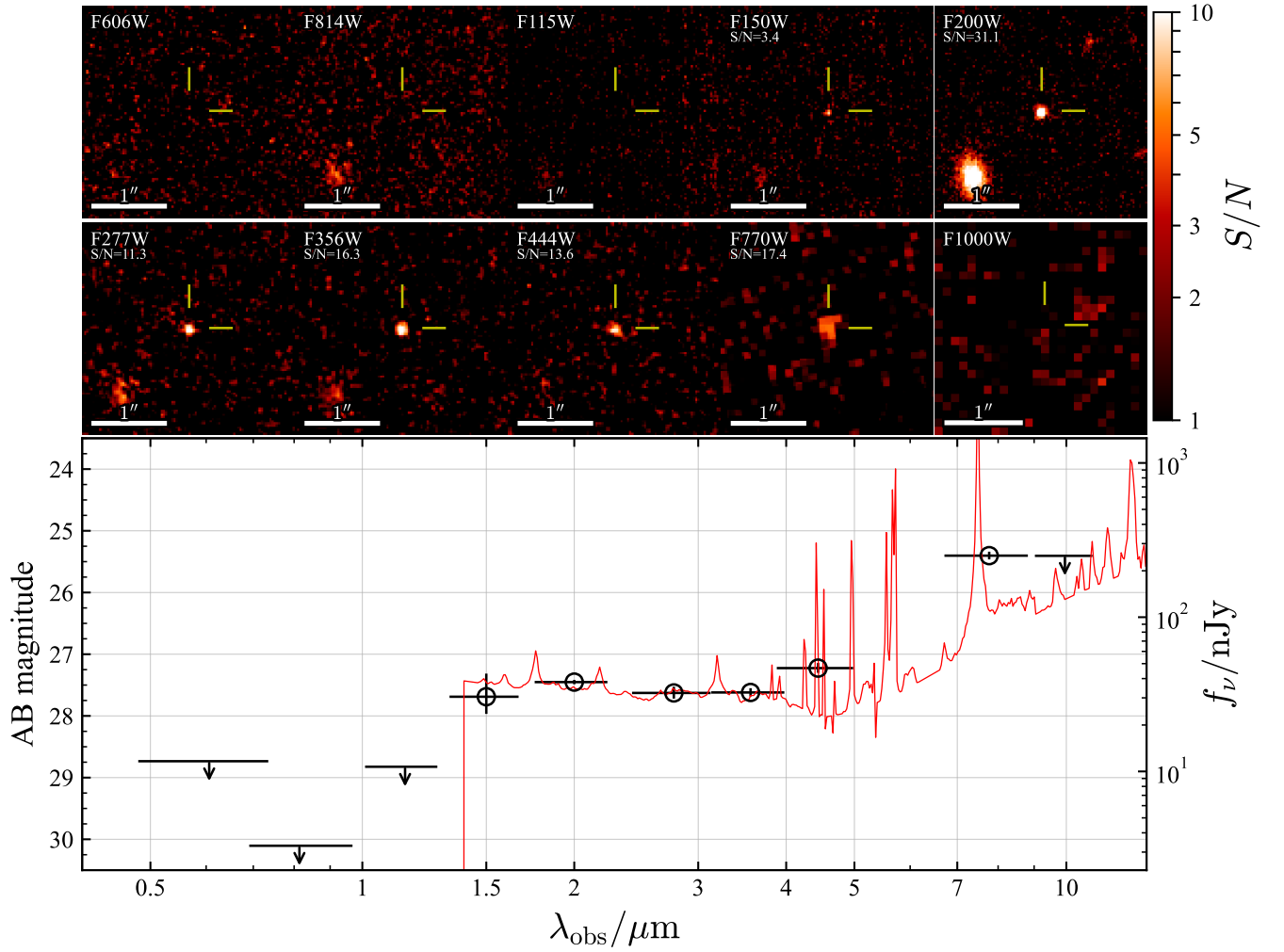
Figure 3. Upper panels: HST + JWST $3'' \times 3''$ cutout images centered on CW-LRD-z10. Each image is scaled by a noise map. If detected, the S/N measured from forced photometry is shown in the top-left corner. Lower panels: observed SED of CW-LRD-z10. For F606W, F814W, F115W, F1000W, and F2100W, we plot the 2σ upper limits. The red line indicates the best-fit LRD model SED from the SED fitting analysis (Section 4.2)

To select compact sources, we compare aperture photometry measured in $0''\!.2$ and $0''\!.5$ apertures on F444W images:

$$\text{compactness} = \frac{f_{\text{F444W}}(0''\!.2)}{f_{\text{F444W}}(0''\!.5)}. \qquad (4)$$

Then, we require the compactness to be between 0.5 and 0.7 following H. B. Akins et al. (2024), where the lower and upper limits exclude extended objects and imaging artifacts, respectively. The corresponding rest-frame wavelength of F444W at $z \sim 10$ ($\sim 0.4\,\mu$m) is shorter than at $z \sim 6$ ($\sim 0.6\,\mu$m), which is the median photometric redshift of the sample in H. B. Akins et al. (2024). However, F444W still probes the rest-frame optical regime, longer than the Balmer limit. Additionally, F770W has lower spatial resolution compared to F444W. Therefore, we continue to use F444W for compactness measurements. We also confirm in Section 5.2 that the selected source is compact in other JWST filters.

We identify six objects after applying the aforementioned selection based on S/N, color, and compactness. Visual inspection of their images reveals that four of these are indistinguishable from noise or artifact patterns in F770W. Another object shows tentative detections in both the HSC and HST F435W images. Therefore, five objects are excluded with their cutout images shown in Appendix B.

As a result, we find one LRD candidate at $z \sim 10$ (CW-LRD-z10; ID: 426069 in COSMOS2025). The images and SED of this object are shown in Figure 3, and its key information is summarized in Table 2.

Since compactness can be underestimated in LRDs with companions (T. S. Tanaka et al. 2024), we also implement a relaxed compactness interval 0.4–0.7, which provides no additional candidates. Note that `warn_flag = 2` and `3` in COSMOS2025 indicate cases where UVISTA fluxes significantly exceed the fluxes in the nearest NIRCam bands and those that are expected to be detected in HSC or UVISTA based on their NIRCam photometry but are not detected, respectively. These cases are primarily due to blending with nearby brighter objects in the UVISTA or HSC images (M. Shuntov et al. 2025). We confirm that none of the objects with `warn_flag = 2` or `3` are selected with our method, even if we do not apply an S/N cut in the HSC bands.

3.3. Comparison with Previous Studies

The following objects, previously selected as high-z LRD candidates in the COSMOS-Web field, are not selected in our study for various reasons.

1. Among the sources selected in H. B. Akins et al. (2024) with the color threshold of $m_{\text{F277W}} - m_{\text{F444W}} > 1.5$, two

Table 2
Properties of CW-LRD-z10

Property	Value
ID in COSMOS2025	426069
R.A.	150°.0840984
	($10^h00^m20^s.1836$)
Decl.	2°.453895
	($2° 27' 14''.022$)
f_{F606W}/nJy	<12
f_{F814W}/nJy	<3.3
f_{F115W}/nJy	<11
f_{F150W}/nJy	30.5 ± 8.9
f_{F200W}/nJy	37.9 ± 1.2
f_{F277W}/nJy	32.3 ± 2.9
f_{F356W}/nJy	32.5 ± 2.0
f_{F444W}/nJy	46.8 ± 3.4
f_{F770W}/nJy	$(2.51 \pm 0.14) \times 10^2$
f_{F1000W}/nJy	$<2.5 \times 10^2$
f_{F2100W}/nJy	$<1.6 \times 10^3$
z_{photo}	$10.50^{+0.72}_{-0.58}$
M_{UV}	$-19.9^{+0.1}_{-0.2}$

Note. Magnitudes are measured using PSF-matched photometry with aperture correction. Upper limits are based on the 2σ noise level in the corresponding aperture. z_{photo} is from the type-I AGN model from H. B. Akins et al. (2024).

objects, ID:49687 and ID:77439 (IDS are from COS-MOS2025[73]), satisfy our color conditions (Equations (1), (2), and (3)) as shown in red diamonds in Figure 2. ID:49687 is detected in F115W (S/N = 5.4) and in HSC (S/N = 4.6 in the g band) and, thus, does not pass the S/N cut and is likely a low-z object. On ID:77439, while the photometric redshift ($z_{\mathrm{photo}} = 8.5^{+3.0}_{-3.6}$), given in COSMOS2025 is consistent with $z \sim 10$, it is barely detected in F150W (S/N = 2.1); hence, it does not pass the S/N cut. Even if ID:77439 is a genuine $z \sim 10$ LRD, M_{UV} would be -18.5 (based on F150W photometry), much lower than our targeted luminosity range; thus, it does not affect our final discussion about the LRD luminosity function at $z \sim 10$ (Section 6.1).

2. CAPERS-LRD-z9 at $z_{\mathrm{spec}} = 9.288$ (A. J. Taylor et al. 2025b) lies within PRIMER-COSMOS, which overlaps with the COSMOS-Web field and is deeper than COSMOS-Web by ~ 1 mag. However, CAPERS-LRD-z9 is out of the MIRI/F770W coverage; thus, it is not selected with our method. Also, note that CAPERS-LRD-z9 has $M_{\mathrm{UV}} = -18.2$, which is fainter than our target luminosity range of $M_{\mathrm{UV}} \lesssim -19.5$ limited by the F150W depth in COSMOS-Web (Figure 1 and Section 3.2). CAPERS-LRD-z9 with $m_{\mathrm{F150W}} = 29.12$ is indeed detected in the F150W observation in PRIMER-COSMOS; however, it is not detected in COSMOS-Web with a shallower F150W depth than PRIMER-COSMOS. Therefore, even if it had been covered by F770W, it would have not passed the S/N cut.

3. D. D. Kocevski et al. (2025) selected four objects as $z_{\mathrm{photo}} > 10$ LRD candidates using only NIRCam photometry from PRIMER-COSMOS (see Appendix A).

---

[73] ID:73111 and ID:88514, respectively, in the H. B. Akins et al. (2024) catalog.

However, three of the four candidates, PRIMER-COS-49611, PRIMER-COS-70533 (CAPERS-LRD-z9 discussed above; A. J. Taylor et al. 2025b), and PRIMER-COS-78729, are not in the parent sample due to the lack of the COSMOS-Web F770W coverage. Also, note that PRIMER-COS-78729 is confirmed to be $z_{\mathrm{spec}} = 5.9$ from archival spectroscopic data (see Appendix A). The remaining source, PRIMER-COS-113415, is faint ($M_{\mathrm{UV}} = -17.58$ if we assume $z_{\mathrm{photo}} = 10.69$) and is not detected in COSMOS2025.

4. Analysis of CW-LRD-z10

We describe the analysis of CW-LRD-z10, our single LRD candidate at $z \gtrsim 10$.

4.1. Forced Photometry

We perform PSF-matched forced photometry of CW-LRD-z10 from HST/F606W to MIRI/F770W, including filters not covered in COSMOS2025, to have uniform photometric measurements. We reconstruct empirical PSFs based on field stars for each band (Section 4.3), and then match the PSFs of all images to the F770W PSF, the longest-wavelength filter (with the largest PSF FWHM) in which CW-LRD-z10 is detected. We measure the photometry using a $0''.54$ diameter circular aperture, which corresponds to $2\times$ the FWHM of the F770W PSF. The surface brightness profile of CW-LRD-z10 is well described by the PSF (Sections 4.3 and 5.2); thus, we perform the aperture photometry with a correction to estimate the total photometry assuming the F770W PSF. For nondetections in F606W, F814W, and F115W, we use error maps to compute the 2σ error on the aperture photometry as an upper limit. The forced photometry is consistent with the PSF photometry estimated from the image-based fitting analysis (Section 4.3) within the 1σ uncertainty. For the nondetections in MIRI (F1000W and F2100W), we do not perform PSF matching to maintain a higher spatial resolution for the detection images. To estimate upper limits in F1000W and F2100W, we use a $0''.66$ and $1''.35$ diameter circular aperture, respectively, which corresponds to $2\times$ each FWHM, and apply an aperture correction assuming each PSF. The resulting photometry and upper limits are listed in Table 2.

4.2. SED Fitting

Using forced photometry, we perform SED fitting to estimate the photometric redshift. We employ the Bayesian SED modeling code BAGPIPES (A. C. Carnall et al. 2018) for the following three setups:

1. The first is a standard galaxy model having stellar mass of $\log(M_*/M_\odot) = 4$–12, stellar metallicity of $Z_*/Z_\odot = 0.1$–1, a delayed-τ star formation history with the timescale (tau) of 0.01–10 Gyr and age of 0.005–10 Gyr, and dust attenuation ($A_V = 0$–8). The upper limit on the age is automatically set to the age of the Universe at each redshift. We also include dust emission and nebular lines with $\log U = -2$. We fit the model in the redshift range of $z = 2$–15. This single high-z galaxy model fitting is intended to confirm whether a normal galaxy SED can reproduce the observed SED. A poor fit would strengthen the interpretation that

CW-LRD-z10 is an LRD, whose SED cannot be reproduced by a standard galaxy model alone, requiring a mixed model such as a dusty galaxy and a normal galaxy (e.g., I. Labbe et al. 2025) or scattered light (H. B. Akins et al. 2024).

2. The second is the same galaxy model as above but limited to the redshift range of $z = 0$–2 to test the $z \sim 0.2$ solution.

3. The final is a type-I AGN model from H. B. Akins et al. (2024) for fitting LRDs ($z = 0$–15), which incorporate a power-law accretion disk, flexible emission-line templates based on M. J. Temple et al. (2021), and dust attenuation with scattering.

By comparing the results with these three cases, we assess the possibility of interlopers or a non-LRD nature (SFGs or Balmer break galaxies). We account for the nondetections in F606W, F814W, F115W, and F1000W by setting the flux to zero and the error to the 1σ upper limit.

Note that the type-I AGN model from H. B. Akins et al. (2024) includes hot torus emission at rest-frame MIR wavelengths, and the red slope is reproduced by invoking strong dust extinction. This may be inconsistent with recent studies reporting a lack of strong hot torus emission (G. Barro et al. 2024b; C. C. Williams et al. 2024; D. J. Setton et al. 2025, B. Wang et al. 2025) and that the rest-frame optical slope of LRDs may be the Wien side of the blackbody emission with $T_{\mathrm{eff}} \sim 5000$ K (K. Inayoshi et al. 2025; D. Kido et al. 2025; H. Liu et al. 2025; X. Lin et al. 2025b). However, the model by H. B. Akins et al. (2024) can well reproduce the SED of LRDs from the rest-UV to rest-optical wavelengths. Therefore, we exclude the F2100W photometry for SED fitting since it falls within the wavelength range where hot torus emission could have a significant impact when using the model by H. B. Akins et al. (2024). Therefore, we only use the available HST, NIRCam, and MIRI (F770W, F1000W) photometry as inputs. Furthermore, we do not use any derived physical parameters other than the photometric redshift (e.g., M_*, star formation rate (SFR), A_V).

4.3. Image-based Fitting

To confirm CW-LRD-z10 as being compact, we conduct image modeling using galight (X. Ding et al. 2020). We fit a cutout image of 101 pixel × 101 pixel centered on CW-LRD-z10 with either a point source or a Sérsic profile (J. L. Sérsic 1963) with $r_e = 0\farcs03$–$0\farcs5$ and $n = 0.5$–5.0.

For PSF reconstruction, we follow the methodology described in T. S. Tanaka et al. (2025). First, we create an empirical PSF library for each filter based on field stars, which contains $\sim$15–40 single PSFs. We test a fit of CW-LRD-z10 assuming each single PSF in the PSF library. Based on these single-PSF results, we sort the single PSFs in the order of χ^2, then we stack the PSFs with the five lowest χ^2 values and the 75% lowest χ^2 values. We use these top-five and the top-75% stacked PSFs as the final PSFs.

To compare the fitting quality with PSF and Sérsic, we calculate the Bayesian information criterion (BIC; G. Schwarz 1978):

$$\mathrm{BIC} = -2\ln L + k \cdot \ln(N), \qquad (5)$$

where L is the maximum likelihood, k is the number of free parameters, and N is the number of data points. With the

assumption of the Gaussian error, we calculate the term of L as $-2\ln L = \chi^2$. Generally, a lower BIC value indicates a better model fit, penalizing excessive model complexity. We compute the difference in BIC as $\Delta \mathrm{BIC} = \mathrm{BIC_{PS}} - \mathrm{BIC_{Sérsic}}$. If the Sérsic model yielded a BIC value lower than the PS model by more than 10 (i.e., $\Delta \mathrm{BIC} > 10$), we consider that the Sérsic model describes the data better than the point-source model. Otherwise, the candidate is unresolved.

5. Results

5.1. V-shape SED

As shown in the Figure 3 (lower panel), the photometry of CW-LRD-z10 indicates a V-shaped SED: almost flat SED from F150W to F356W and a red steep slope from F356W to F770W. This SED is consistent with the photometric redshift of $z \sim 10$ (Section 5.3), because at this redshift, the Balmer limit should shift to $4\,\mu$m and fall in the F444W coverage. However, as discussed in D. D. Kocevski et al. (2025), there are different interpretations of a red color ($m_{\mathrm{F444W}} - m_{\mathrm{F770W}} = 1.82 \pm 0.1$). If we estimate the rest-optical slope from the $m_{\mathrm{F444W}} - m_{\mathrm{F770W}}$ color by simply assuming a power-law continuum, we obtain a value of $\beta = 1.05 \pm 0.18$. Note that the photometry may include contributions from emission lines; thus, the derived slope above may not accurately reflect the intrinsic continuum slope. In this section, we discuss possible non-LRD interpretations of the observed red $m_{\mathrm{F444W}} - m_{\mathrm{F770W}}$ color under different scenarios.

5.1.1. Contribution of Strong Hα

One way to produce a large $m_{\mathrm{F444W}} - m_{\mathrm{F770W}}$ color without a red continuum would be an extremely strong Hα line, which falls into the F770W coverage at $z \sim 10$. However, we rule out this scenario for the following reasons. If we assume a flat continuum SED (constant f_ν at f_{F444W}, i.e., $\beta = -2$) and attribute the entire F770W excess from F444W to Hα emission, the inferred rest-frame Hα EW is $\sim$8000 Å. This EW is significantly larger than those predicted for metal-poor or metal-free galaxies ($\lesssim$4000 Å; A. K. Inoue 2011) or those of extreme emission-line galaxies ($\sim$2000 Å; e.g., S. Withers et al. 2023), making it difficult to explain within the framework of known galaxy populations.

For reference, JADES-GS-z14-0, discovered at $z_{\mathrm{spec}} = 14.32$, was also detected in F770W, and the most reasonable interpretation of this bright F770W photometry is a contribution of strong Hβ+[O III]$\lambda\lambda$4959, 5007 lines (J. M. Helton et al. 2025). However, JADES-GS-z14-0 exhibits a color of $m_{\mathrm{F444W}} - m_{\mathrm{F770W}} = 0.5$ (J. M. Helton et al. 2025), whereas our object shows a color of $m_{\mathrm{F444W}} - m_{\mathrm{F770W}} = 1.8$, suggesting that a different scenario is likely responsible.

If we assume an AGN-like continuum slope of $\beta = -1.5$, an extremely strong Hα with EW of $\sim$6000 Å is still needed to reproduce the color, which significantly exceeds the predicted EWs for a seed BH ($\sim$1300 Å; K. Inayoshi et al. 2022). In contrast, assuming a steeper slope of $\beta = 0.5$ as typically observed in LRDs (e.g., J. E. Greene et al. 2024; X. Lin et al. 2025a) yields a more plausible EW of 800 Å, consistent with the EWs of known LRDs (e.g., D. J. Setton et al. 2024; R. Maiolino et al. 2025).

5.1.2. Balmer Break

If the Balmer break were extremely strong, it could produce a flux change around $4\,\mu$m. However, we can rule out the

scenario in which a stellar population reproduces such a strong break, which matches the observed color. Here, we simply model the SED of a Balmer break galaxy as a flat-f_ν spectrum with a sharp, wall-like break at a rest-frame wavelength of 0.3646 μm, and quantify the strength of the break using the f_ν ratio across the break. If the observed color of $m_{\rm F356W} - m_{\rm F770W} = 2.22$ in CW-LRD-z10 is fully described by the Balmer break, the implied Balmer break strength is 7.6, which significantly exceeds the upper limit ($\sim$3) expected for normal stellar populations (e.g., A. de Graaff et al. 2025; K. Inayoshi & R. Maiolino 2025; R. P. Naidu et al. 2025a).

Such extremely strong Balmer breaks are found in some LRDs (I. Labbe et al. 2024; C. C. Williams et al. 2024; A. de Graaff et al. 2025; X. Ji et al. 2025b; R. P. Naidu et al. 2025a). However, we can rule out this scenario for CW-LRD-z10 because it does not show $m_{\rm F277W} - m_{\rm F444W}$ and $m_{\rm F444W} - m_{\rm F770W}$ colors as large as the SED of The Cliff, as shown in Figure 2 (right panel). This is also evident in Figure 3 (lower panel), which indicates that the observed SED of CW-LRD-z10 clearly does not match that of The Cliff (A. de Graaff et al. 2025).

Therefore, to explain the red color observed in CW-LRD-z10 across the 4–7 μm, a rest-optical steep continuum slope as found in typical LRDs is required. This conclusion is also consistent with the fact that the SED could not be well reproduced by a single galaxy model using BAGPIPES as described in Section 5.3.

5.2. Compact Morphology

As described in Section 4.3, we perform image-based morphological fitting across all filters from F150W to F770W where CW-LRD-z10 is detected. In every band and for both the top-five and the top-75% PSFs, the point-source model results in a lower BIC than the Sérsic profiles. This result strongly supports the interpretation that the object is compact and unresolved at JWST resolution. This compactness is further and independently confirmed in the flux–FWHM plane (Appendix C), where CW-LRD-z10 follows the same sequence as the point-source objects. The lower limit on the effective radius in our image-based fitting is 0″03, and we use this value as an upper limit for the effective radius. The upper limit corresponds to a projected size of $\lesssim$120 pc at $z \sim 10$, consistent with the size constraints of previous LRDs (e.g., L. J. Furtak et al. 2023; H. B. Akins et al. 2024; J. F. W. Baggen et al. 2024).

Recent high-redshift observations suggest that galaxies at $z \gtrsim 10$ can be broadly divided into two populations: compact galaxies with strong N IV], and spatially extended galaxies with weak N IV] (Y. Harikane et al. 2025; R. P. Naidu et al. 2025b). Our size upper limit is smaller than the typical rest-UV circularized half-light radius of the high-z galaxy population ($\sim$200 pc; Y. Ono et al. 2025), and is instead consistent with the compact galaxy population ($\lesssim$100 pc). Therefore, at least, CW-LRD-z10 is morphologically distinct from the extended high-z galaxy population.

One extreme hypothesis that might be considered here is that all of the high-z compact population corresponds to LRDs. However, spectroscopically compact $z > 10$ objects have distinct features from LRDs. For example, GN-z11 and GHZ-2 do not show broad Hα emission lines (J. Álvarez-Márquez et al. 2025; J. A. Zavala et al. 2025), MoM-z14 shows morphologies more extended than the PSF (R. P. Naidu et al.

2025b), and GS-z14-1 does not show F770W excess compared to NIRCam photometry (Z. Wu et al. 2025). Thus, this interpretation is unlikely.

If CW-LRD-z10 is a dwarf galaxy at $z \sim 0.2$, the corresponding size limit would be $\lesssim$100 pc. Typical dwarf galaxies with $M_* \sim 10^6 M_\odot$ in the local Universe have effective radii of several hundred parsecs (e.g., M. A. Norris et al. 2014), which would be inconsistent with this upper limit on its size. Therefore, the size constraint disfavors typical extended dwarf galaxy solutions. However, in the case of ultra-compact dwarf galaxies, the observed size constraint would remain consistent with $\lesssim$100 pc (e.g., M. A. Norris et al. 2014).

5.3. Photometric Redshift

The SED of the selected object exhibits a distinct V-shaped feature with a trough around F356W, consistent with the model SED of $z = 10$ LRDs shown in Figure 1. Additionally, the SED shows a flux discontinuity between F115W and F150W, consistent with the Lyman break falling between those filters, further supporting $z \sim 10$. While a typical dropout selection technique uses colors based on forced photometry such as $m_{\rm F115W} - m_{\rm F150W}$ or performs SED fitting in the selection stage, we apply only S/N cuts to select F115W-dropout objects (Section 3.2); thus, our dropout selection is looser compared to other dropout selections (e.g., Y. Harikane et al. 2023b; C. M. Casey et al. 2024; M. Franco et al. 2024). However, CW-LRD-z10 still passes the color criteria for F115W-dropout galaxies proposed by Y. Harikane et al. (2023b; gray-filled region in Figure 2, left panel). Also, note that our selection does not rely solely on the F115W dropout, but also incorporates a requirement for a significant slope change across the Balmer limit around $\sim$4 μm, which is a distinctive feature of LRDs. As illustrated by the green hexagon in Figure 2 (right panel), a $z \sim 2.5$ Balmer break galaxy, a typical interloper in F115W-dropout selection, occupies a markedly different location from $z \sim 10$ LRDs in the $m_{\rm F277W} - m_{\rm F444W}$ versus $m_{\rm F444W} - m_{\rm F770W}$ color–color plane, especially in $m_{\rm F444W} - m_{\rm F770W}$. Thus, using both features makes our selection robust against $z \sim 2.5$ Balmer break galaxies.

We test this $z \sim 10$ LRD scenario through the SED fitting analysis described in Section 4.2. The χ^2 distribution and the best-fit model SED are shown in Figure 4. When fitting over the wide redshift range of $0 < z < 15$ with the type-I AGN model from H. B. Akins et al. (2024), we obtain a best-fit photometric redshift of $z_{\rm photo} = 10.50^{+0.72}_{-0.58}$. Then, when fitting over the low-redshift range of $0 < z < 2$ with the galaxy model, we obtain a best-fit photometric redshift of $z_{\rm photo} = 0.23^{+0.02}_{-0.01}$. The $z \sim 10$ LRD solution has much lower χ^2 with $\Delta\chi^2 = 33.7$ than the $z \sim 0.2$ galaxy solution (see Figure 4). The discrepancy between the observed photometry and the $z \sim 0.2$ galaxy SED is particularly evident in F1000W, where the predicted flux density in the $z \sim 0.2$ galaxy solution exceeds the observed upper limit due to the contribution from the PAH 7.6 μm feature. In the $z \sim 0.2$ galaxy case, the F115W dropout is attributed to the rest-optical-to-NIR dust-obscured continuum; however, this explanation fails, and it predicts brighter F814W and F115W photometry than the observed upper limits, resulting in further inconsistencies. Thus, we conclude that the $z \sim 0.2$ galaxy case cannot reproduce the observed photometry for CW-LRD-z10.
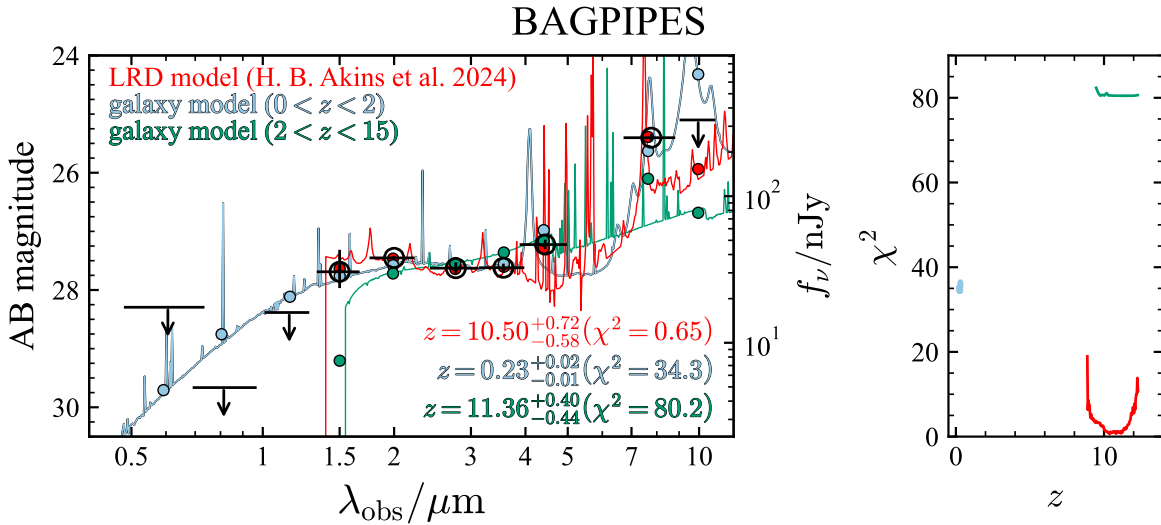
Figure 4. Observed photometry and SED fitting results using BAGPIPES. In the left panel, black open circles, small dots, and lines represent the observed photometry, the model photometry, and the model SEDs. The estimated z_{photo} and corresponding χ^2 value for each fit are indicated in the lower-right corner. The right panel shows the χ^2 distribution as a function of redshift. Red, cyan, and green lines indicate fits using the LRD model from H. B. Akins et al. (2024) over $0 < z < 15$, the galaxy model over $0 < z < 2$, and the galaxy model over $2 < z < 15$, respectively.

Fitting over the high-redshift range of $2 < z < 15$ with the galaxy model yields photometric redshifts of $z_{photo} = 11.36^{+0.40}_{-0.44}$ and higher χ^2 values than the $z \sim 10$ LRD solution ($\Delta\chi^2 = 79.6$). BAGPIPES assumes a single galaxy population, and the resulting best-fit SED includes strong emission lines. However, the high-redshift galaxy model fails to simultaneously reproduce both the rest-frame UV part and the rest-optical flux excesses in F444W and F770W. This result suggests that the SED of CW-LRD-z10 is difficult to reconcile with a typical single-component galaxy model. Therefore, we conclude that CW-LRD-z10 is highly likely to be an LRD at $z_{photo} = 10.50^{+0.72}_{-0.58}$, rather than a normal galaxy at $z \sim 0.2$ or $z \sim 10$.

5.4. UV Luminosity

If the photometric redshift is correct, CW-LRD-z10 would be one of the most distant SMBHs ever detected, comparable to GHZ-9 ($z_{spec} = 10.145 \pm 0.010$; O. E. Kovács et al. 2024; L. Napolitano et al. 2025), UHZ-1 ($z_{spec} = 10.073 \pm 0.002$; A. D. Goulding et al. 2023; Á. Bogdán et al. 2024), and GN-z11 ($z_{spec} = 10.6034 \pm 0.0013$; P. A. Oesch et al. 2016; L. Jiang et al. 2021; A. J. Bunker et al. 2023; R. Maiolino et al. 2024b). Assuming the photometric redshifts derived from the fits using the LRD model, we estimate the UV absolute magnitude using

$$M_{UV} = m_{1450(1+z)} - 5\log_{10}\left(\frac{D_L}{10\ pc}\right) + 2.5\log_{10}(1+z), \quad (6)$$

where D_L is the luminosity distance, and $m_1450(1+z)$ is the rest-frame 1450 Å magnitude inferred from the best-fit model SED. The resulting UV absolute magnitude is $M_{UV} = -19.9^{+0.1}_{-0.2}$. These results are further supported by the SED fitting performed with EAZY (G. B. Brammer et al. 2008), as detailed in Appendix D. We also note that, given the lack of a definitive conclusion regarding the level of dust extinction in LRDs, we do not apply any correction for dust attenuation. Therefore, the intrinsic UV absolute magnitude may be smaller than the value derived here.

5.5. Nondetection in Multiwavelength Data

CW-LRD-z10 was also covered and not detected by Atacama Large Millimeter/submillimeter Array (ALMA) Band 6 (~ 250 GHz) with a continuum sensitivity of 0.167 mJy beam^{-1} (CHAMPS ALMA program, ID: 2023.1.00180.L, PI: A. Faisst; A. Faisst et al. 2025, in preparation). Based on the $z \sim 0.2$ dusty dwarf SFG model SED, the expected continuum flux at ALMA Band 6 is 1.1 μJy, respectively, which falls significantly below the sensitivity limit. Therefore, this ALMA result does not rule out the $z \sim 0.2$ solution.

We also check the Chandra/ACIS-I (COSMOS Chandra Merged Image Data Version 1.0, F. Civano et al. 2016) and VLA 3 GHz (VLA-COSMOS, V. Smolčić et al. 2017), both downloaded from the COSMOS dataset in Infrared Processing and Analysis Center (IPAC; COSMOS Project 2020[74]). CW-LRD-z10 is not detected in either image. Chandra observations have the limiting depth of 2.2×10^{-16} erg cm^{-2} s^{-1} in the 0.5–2 keV band, and the VLA 3 GHz observation has the 1σ sensitivity of 2.3 μJy beam^{-1}. These nondetections are consistent with previous studies that have reported the absence of X-rays (H. B. Akins et al. 2024; T. T. Ananna et al. 2024; M. Yue et al. 2024; X. Lin et al. 2025b; R. Maiolino et al. 2025; A. Sacchi & A. Bogdan 2025) and radio (H. B. Akins et al. 2024; G. Mazzolari et al. 2024; X. Lin et al. 2025b; K. Perger et al. 2025) emission in LRDs.

5.6. Grism Spectra

As described in Section 2.4, CW-LRD-z10 has been observed by COSMOS-3D grism spectroscopy with NIRCam/F444W. F444W (3.86–4.99 μm) can cover [O II] $\lambda\lambda$3726,3729, [Ne III]λ3869, [Ne III]λ3967, and Hδ for a galaxy or LRD at $z \sim 10$ and the PAH 3.3 μm for a $z \sim 0.2$ galaxy. However, CW-LRD-z10 with $m_{F444W} = 27.2$ is too faint to be detected in the COSMOS-3D spectrum, and indeed, the resulting data show no significant line detections. For

---

comparison, X. Lin et al. (2025a) reported line detections with line flux S/N > 2 only for sources with $m_{F444W} < 26$.

We conduct a mock observation based on the model SED shown in Figure 4 with the JWST ETC.[75] The estimated S/N is < 0.1 even at the peak of [O II]$\lambda\lambda$3726,3729 in the best-fit LRD and galaxy model SED or the PAH 3.3 μm feature in the best-fit $z \sim 0.2$ galaxy model. Therefore, while the lack of emission-line detection is consistent with our SED fitting analysis, we cannot obtain any strong constraints on its redshift and nature from the current grism data. Deeper follow-up spectroscopy will be essential to robustly confirm the redshift and the nature of this object.

6. Discussion

6.1. Luminosity Function and Evolution of the LRD Population

We loosely constrain the number density of the LRD at $z \sim 10$ by assuming that CW-LRD-z10 is a genuine LRD at $z_{photo} = 10.5^{+0.7}_{-0.6}$ with $M_{UV} = -19.9^{+0.1}_{-0.2}$ based on the results presented in the previous section.

We first evaluate the completeness of our selection, $C(M_{UV}, z)$, as a function of z and M_{UV} to estimate the luminosity function. We use the stacked model SED of LRDs from H. B. Akins et al. (2024; shown in Figure 1) with a given M_{UV} and evolve the model SED from $z = 5$ to $z = 15$. We then add photometric errors comparable to those in COSMOS-Web to these model SEDs to simulate mock observed photometry. We check whether the mock photometry satisfies the selection criteria: S/N < 2 in F115W, S/N > 5 in F150W, F277W, F444W, and F770W, and color selections (Equations 1–3). We evaluate completeness at three magnitude limits, $M_{UV} = -21$, -20, and -19. For each (M_{UV}, z) combination, we perform Monte Carlo simulations with 10,000 samples to estimate $C(M_{UV}, z)$. Since the COSMOS-Web observations are mosaicked, the actual depth varies across the field (see C. M. Casey et al. 2023; M. Franco et al. 2025a; S. Harish et al. 2025). In this study, we assume the depth distribution across the entire COSMOS-Web field and estimate the completeness for each depth accordingly.

The resulting completeness curves (only for the deepest regions) are shown in Figure 5. Due to the limited survey depth, the completeness for $M_{UV} = -19$ remains ~0 across all redshifts, consistent with the our targeted luminosity range of $M_{UV} \lesssim -19.5$. Since our selection is based on the F115W-dropout criterion, the method becomes sensitive at $z \gtrsim 9$ and achieves a completeness of ~1 around $z \sim 10$ for sources with $M_{UV} = -20$ and -21. For $M_{UV} = -20$ (-21), the completeness declines rapidly above $z \sim 10$ ($z \sim 11$) as the LRDs become too faint to be detected in F150W.

We calculate the effective survey volume $V_{eff}(M_{UV})$ for each M_{UV} as

$$V_{eff}(M_{UV}) = \int C(M_{UV}, z) \frac{dV(z)}{dz} dz, \qquad (7)$$

where dV/dz is the differential comoving volume and $C(M_{UV}, z)$ is the completeness as evaluated above. Based on this effective volume, we estimate the UV luminosity function
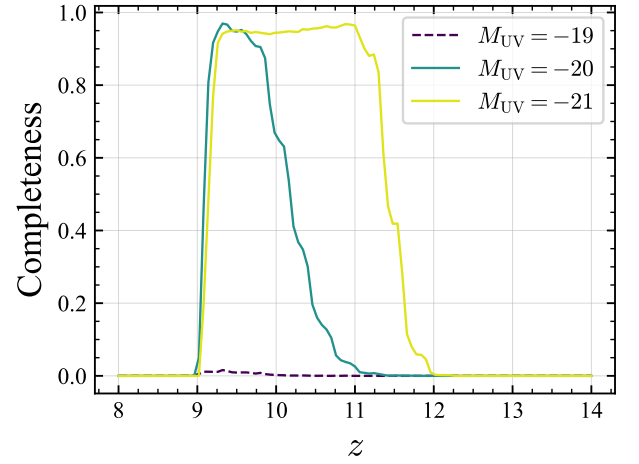
Figure 5. Completeness as a function of redshift and UV absolute magnitude, estimated from a Monte Carlo simulation of COSMOS-Web mock observations.

Table 3
Estimated UV Luminosity Function of $z \sim 10$ LRD ($z = 9$–12)

M_{UV}	bin	$\Phi_{LRD}(M_{UV})$/Mpc^{-3} mag^{-1}
-20	$[-20.5, -19.5]$	$(1.2^{+2.7}_{-1.0}) \times 10^{-6}$
-21	$[-21.5, -20.5]$	$< 5.2 \times 10^{-7}$

**Note.** Uncertainty and upper limits are 1σ assuming Poisson statistics (N. Gehrels 1986).

of LRDs, $\Phi(M_{UV})$, using

$$\Phi_{LRD}(M_{UV}) = \frac{N_{LRD}(M_{UV})}{V_{eff}(M_{UV})}, \qquad (8)$$

where $N_{LRD}(M_{UV})$ is the number of LRD candidates with M_{UV}. We estimate the luminosity function in three bins of $[-21.5, -20.5]$ and $[-20.5, -19.5]$. We evaluate the uncertainty based on Poisson statistics for the small number of objects (N. Gehrels 1986). For the $M_{UV} = -21$ bin where no candidates are identified, we adopt an upper limit at the 1σ (84%) confidence level based on Poisson statistics (N. Gehrels 1986). The results are summarized in Table 3.

Based on the effort in previous studies, we place constraints on the luminosity function at $M_{UV} = -18.2$ for the same redshift range ($9 < z < 12$). As introduced in Section 1, CAPERS-LRD-z9 was photometrically selected in D. D. Kocevski et al. (2025) and spectroscopically confirmed in A. J. Taylor et al. (2025b). D. D. Kocevski et al. (2025) derived the luminosity function using the V_{max} method (M. Schmidt 1968). Following this approach and assuming that only CAPERS-LRD-z9 was detected within the survey area by D. D. Kocevski et al. (2025) at $9 < z < 12$, the inferred number density would be $\Phi_{LRD}(-18.2) > 8 \times 10^{-7}$ Mpc^{-3} mag^{-1}. Since D. D. Kocevski et al. (2025) detected other $z > 10$ LRD candidates with similar luminosities ($M_{UV} \sim -18$) that have not yet been spectroscopically confirmed, we consider this estimate as a lower limit on the low-luminosity side, and use it for comparison with our main results at $M_{UV} < -19.5$.
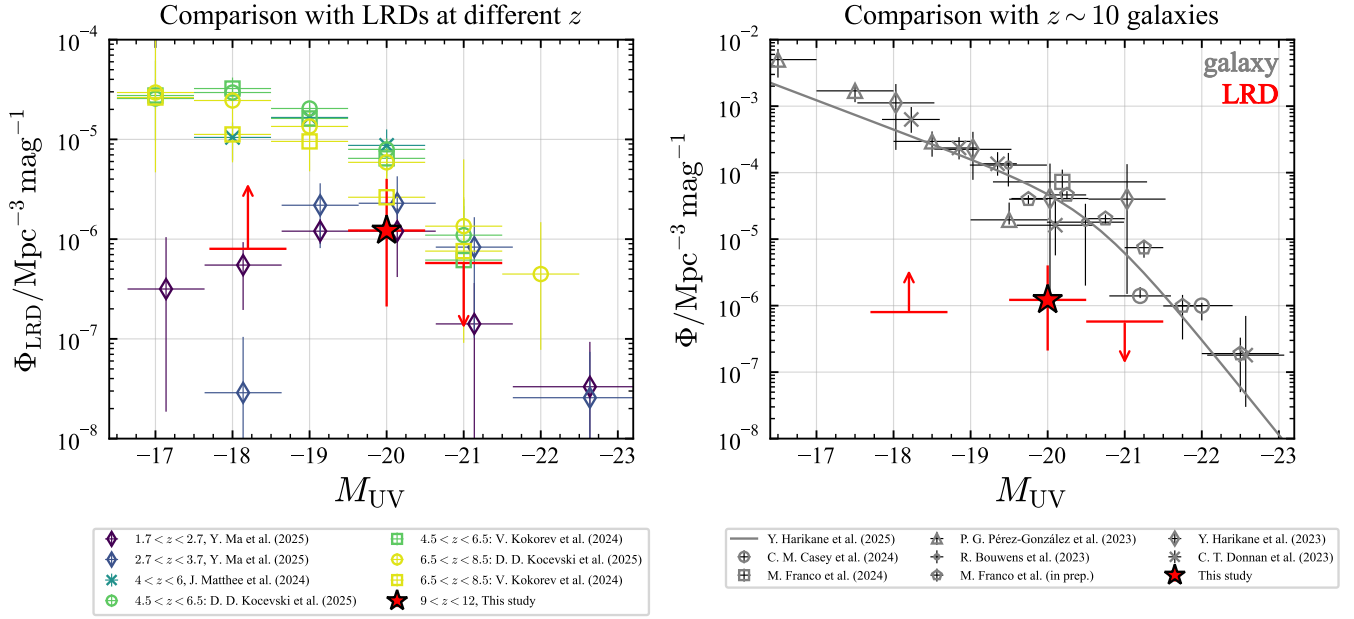
Figure 6. Luminosity function of $z \sim 10$ LRDs shown by the red star data point. Left panel: comparison with the luminosity functions of LRDs at lower redshifts ($1.7 < z < 8.5$) from previous studies (V. Kokorev et al. 2024a; J. Matthee et al. 2024; D. D. Kocevski et al. 2025; Y. Ma et al. 2025b). Note that the lower limit at $M_{UV} = -18.2$ and $9 < z < 12$ is based on the assumption that only CAPERS-LRD-z9 (A. J. Taylor et al. 2025b) is a true $z \sim 10$ LRD in the selection by D. D. Kocevski et al. (2025), independently identified of the selection in this study. Right panel: comparison of the LRD luminosity function with that of galaxies at $z \sim 10$ (R. Bouwens et al. 2023; C. T. Donnan et al. 2023; Y. Harikane et al. 2023b; P. G. Pérez-González et al. 2023; C. M. Casey et al. 2024; M. Franco et al. 2024, 2025b). The best-fit double power-law model from Y. Harikane et al. (2025) is indicated by the black line.

Figure 6 (left panel) presents the UV luminosity function of LRDs at $z \sim 10$ (red) with comparison to those at lower redshifts ($1.7 < z < 8.5$) from previous studies (V. Kokorev et al. 2024a; J. Matthee et al. 2024; D. D. Kocevski et al. 2025; Y. Ma et al. 2025b). Y. Ma et al. (2025b) provided the luminosity function with respect to the rest-frame 5500 Å magnitude (M_{5500}); thus, we apply a correction of $M_{UV} = M_{5500} + 1.86$ assuming the model SED from H. B. Akins et al. (2024). The aforementioned studies have found that the luminosity function of LRDs increases from $z \sim 2$ to $z \sim 6$, followed by a slight decline to $z \sim 8$. While we have only a single bin of $M_{UV} = -20$ at $z = 10$, the luminosity function at $M_{UV} = -20$ is found to be lower than that at $z = 6.5$–8.5 (D. D. Kocevski et al. 2025) by $0.7^{+0.7}_{-0.5}$ dex.

This redshift evolution is further illustrated in Figure 7, where the comoving space density at $M_{UV} = -20$ is plotted as a function of z. We fit the redshift evolution of the LRD luminosity function at $M_{UV} = -20$ from our study and previous studies (V. Kokorev et al. 2024a; J. Matthee et al. 2024; D. D. Kocevski et al. 2025; Y. Ma et al. 2025b; M.-Y. Zhuang et al. 2025[76]) with the log-normal distribution recently proposed by K. Inayoshi (2025), expressed as:

$$\Phi_{LRD}(z) = \Phi_{0,LRD} f(z)$$
$$\times \exp\left[-\frac{\{\ln(1+z) - \ln(1+z_0)\}^2}{2\sigma_z^2}\right], \quad (9)$$

$$f(z) = \frac{(1+z)^{\frac{3}{2}}}{(s(1+z)^{\frac{1}{2}} - 1)^2}, \quad (10)$$

where $\Phi_{0,LRD}$ is the normalization of the log-normal distribution, z_0 is the peak redshift, and σ_z represents the width
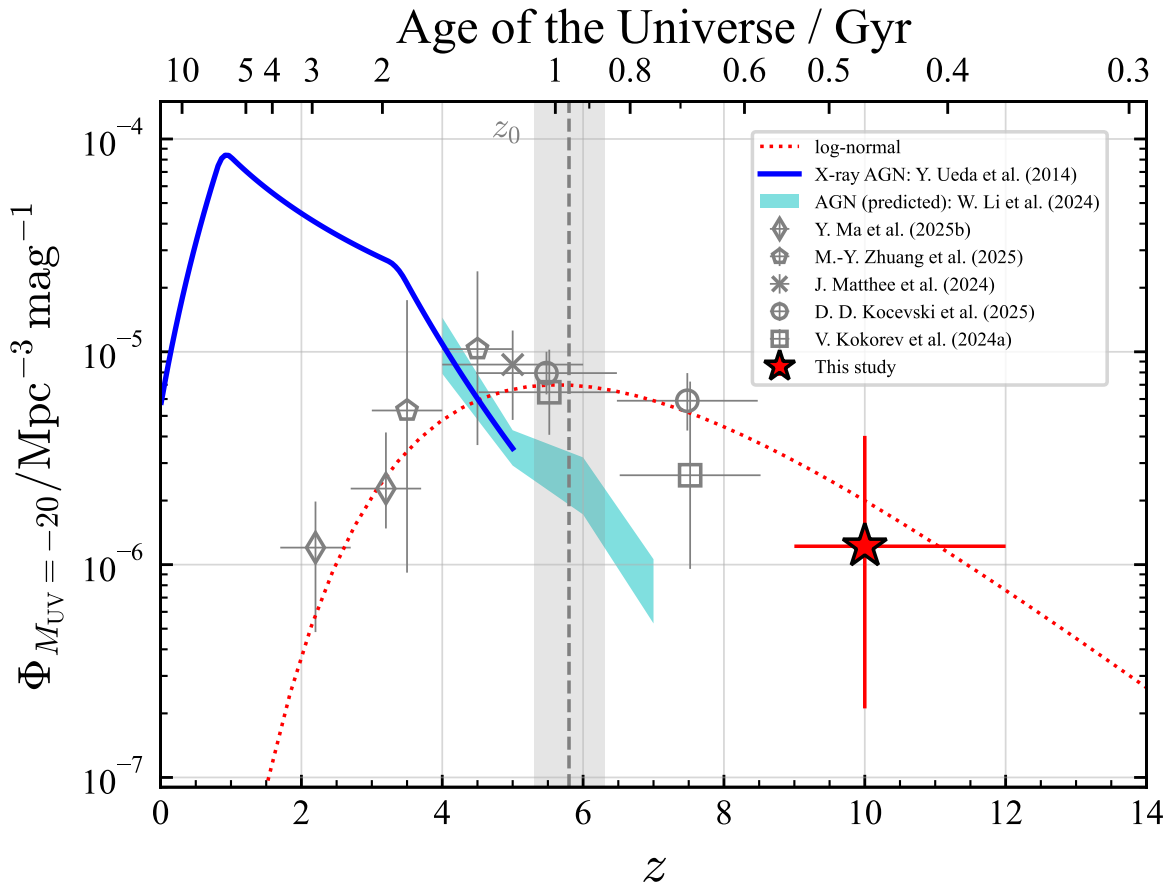
of the distribution. The function $f(z)$ accounts for the redshift dependence of both the differential comoving volume element dV/dz and the cosmic time interval dt/dz. We adopt $s = 0.901$, corresponding to the assumed flat cosmology with $\Omega_m = 0.3$ and $\Omega_\Lambda = 0.7$. The estimated parameters are $\Phi_{0,LRD} = (7.4^{+1.5}_{-1.5}) \times 10^{-7}$ Mpc^{-3} mag^{-1}, $z_0 = 5.8^{+0.6}_{-0.5}$, and $\sigma_z = 0.31^{+0.08}_{-0.06}$. As shown in Figure 7, the fitted log-normal distribution agrees well with the observed evolution, within the uncertainty. The consistency with a log-normal distribution may support the scenario proposed in K. Inayoshi (2025) in which the emergence of LRDs is closely linked to stochastic phenomena, for example, the initial accretion of seed BHs. Such an interpretation, linking LRDs to seed BHs, is also consistent with the discovery of an LRD at $z \sim 10$, which indicates that LRDs were already present $\sim$0.5 Gyr after the Big Bang.

While our log-normal fit is based only on the $M_{UV} = -20$ luminosity bin, K. Inayoshi (2025) fitted the same functional form to all LRDs with $M_{UV} < -18$, obtaining a slightly higher peak redshift $z_0 = 6.53^{+0.04}_{-0.03}$ and a narrower width $\sigma_z = 0.218 \pm 0.005$. As seen in Figure 6 (left panel), the luminosity functions at $z \lesssim 4$ from Y. Ma et al. (2025b) have peaks around $M_{UV} \sim -20$ and concentrate more on the luminous side than those at $z \gtrsim 4$. Consequently, when fitting only the $M_{UV} = -20$ bin, the relatively higher values at $z \lesssim 4$ may make z_0 lower and σ_z broader than the result in K. Inayoshi (2025). This suggests that the shape of the luminosity function of LRDs is redshift-dependent, possibly indicating that either the physical conditions of accretion (i.e., Eddington ratio) in LRDs or the mass function of the LRD population evolves with redshift.

Recently, R. E. Hviding et al. (2025) suggested that while the contamination rate in photometrically selected LRDs is low ($\lesssim$10%), the completeness may be as low as $\sim$50% when compared to spectroscopically confirmed samples. While we apply

---

[76] For M.-Y. Zhuang et al. (2025), we estimate the number density using their sample with $-19.5 < M_{UV} < -20.5$.

Figure 7. Redshift evolution of the luminosity function at $M_{UV} = -20$. Symbols for lower-redshift LRDs (V. Kokorev et al. 2024a; J. Matthee et al. 2024; D. D. Kocevski et al. 2025; Y. Ma et al. 2025b; M.-Y. Zhuang et al. 2025) are the same as in Figure 6 (left panel). The red dotted line indicates the best-fit log-normal distribution. The gray dashed line and shaded region indicate the best-fit peak redshift (z_0). The blue line and cyan shaded region indicate the AGN luminosity function at $M_{UV} = -20$ from the X-rays (Y. Ueda et al. 2014) and model prediction (W. Li et al. 2024). Note that we assume an X-ray-UV luminosity ratio (E. Lusso & G. Risaliti 2016) and a photon index of $\Gamma = 1.9$ to convert the X-ray (Y. Ueda et al. 2014) to UV luminosity function.

a completeness correction by calculating the effective survey volume in Section 6.1, it is important to note that this completeness estimate implicitly assumes the stacked SED of photometrically selected LRDs from H. B. Akins et al. (2024). Therefore, the completeness with respect to the overall LRD population, particularly those with diverse or atypical SEDs, remains uncertain. If the uncertainty in completeness is as large as the ~50% as suggested by R. E. Hviding et al. (2025), our inferred luminosity function could be underestimated by up to a factor of 2. However, we emphasize that the uncertainty due to the small sample size dominates the overall uncertainty for this analysis. Therefore, a larger sample with future surveys is a crucial next step to better constrain the evolutionary trend toward the early Universe.

6.2. LRD Fraction

Figure 6 (right panel) presents the LRD luminosity function at $z \sim 10$ in comparison to the galaxy luminosity function at similar redshifts (C. T. Donnan et al. 2023; Y. Harikane et al. 2023b; C. M. Casey et al. 2024; M. Franco et al. 2024; Y. Harikane et al. 2025). These allow us to estimate the LRD fraction of the galaxy population at $M_{UV} = -20$ as

$$f_{LRD,M_{UV}=-20}(z) = \frac{\Phi_{LRD,M_{UV}=-20}(z)}{\Phi_{galaxy,M_{UV}=-20}(z)}. \quad (11)$$

For the galaxy luminosity function, we use the fitted results from Y. Harikane et al. (2022a) for $z = 3$–6 and Y. Harikane

et al. (2025) for $z > 6$. At $z \sim 10$, we find that the LRD fraction is $2.6^{+5.9}_{-2.1}\%$. In Figure 8, we show the redshift evolution of f_{LRD}. While Φ_{LRD} peaks around $z \sim 7$, the f_{LRD} increases monotonically from $z = 3$ to $z = 8$. At $z = 10$, despite a large uncertainty, there is no evidence of a sharp decline from $z = 8$. A linear fit with $f_{LRD}(z) = a\log(1 + z) + b$ yields $a = 3.68^{+0.61}_{-0.60}$ and $b = -5.10^{+0.49}_{-0.50}$, suggesting that the LRD fraction could reach $f_{LRD} \sim 10\%$ at $z = 14$, where the current highest z_{spec} objects are found (S. Carniani et al. 2024; R. P. Naidu et al. 2025b).

This increasing trend suggests that, although the number density of LRDs decreases toward higher redshift, as described by the log-normal model (red dotted line in Figure 7), the number density of UV-bright galaxies declines even more rapidly than LRDs, causing the relative fraction of LRDs to increase. We introduce two models, theoretical and empirical ones, to interpret this increasing trend quantitatively.

6.2.1. Theoretical Interpretation

In our theoretical model, we begin with simplified assumptions about the origins and evolution of LRDs and galaxies. First, we assume that the formation rates of $M_{UV} = -20$ LRDs ($\dot{n}_{LRD}$) and galaxies ($\dot{n}_{gal}$) are constant and independent of cosmic time. Second, we assume that galaxies can maintain their luminosity after formation, while LRDs
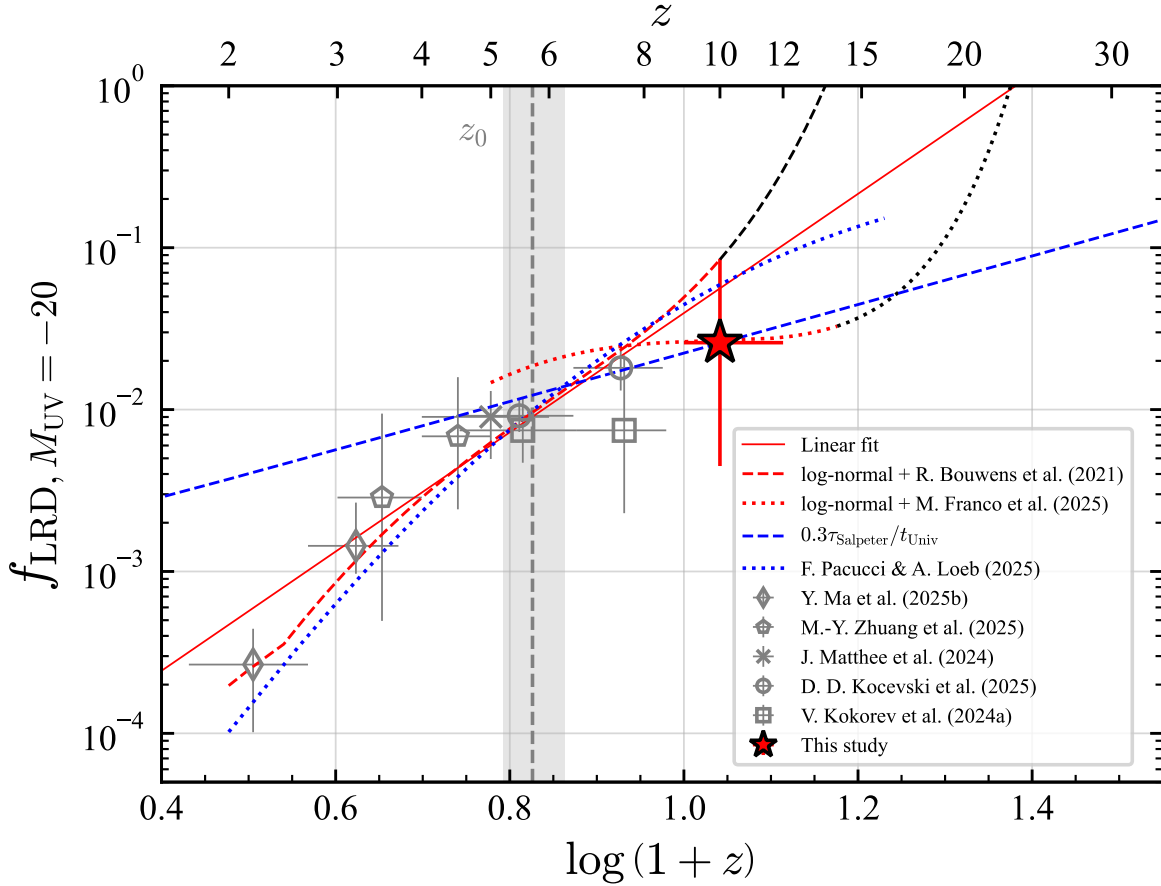
Figure 8. Redshift evolution of the LRD fraction relative to the overall galaxy population at $M_{UV} = -20$. Symbols for lower-redshift LRDs (V. Kokorev et al. 2024a; J. Matthee et al. 2024; D. D. Kocevski et al. 2025; Y. Ma et al. 2025b; M.-Y. Zhuang et al. 2025) are the same as in Figure 6 (left panel). The red solid line shows the best-fit linear model. The red dashed and dotted lines indicate the modeled f_{LRD} redshift evolution that combines the evolutions of the UV luminosity function of LRDs (the fitted log-normal distribution shown in Figure 7) and galaxies from R. J. Bouwens et al. (2021) and M. Franco et al. (2025b), respectively. For each model, the black line indicates the extrapolation of each luminosity function evolution beyond the range constrained by observational data. The blue dashed line indicates 0.3 times Salpeter time ($\tau_{Salpeter}$, with the assumption of $\varepsilon = 0.1$) divided by the age of the Universe (t_{Univ}) at each redshift. The blue dotted line represents the prediction from F. Pacucci & A. Loeb (2025). The gray dashed line and shaded region indicate the fitted peak redshift of the log-normal distribution (z_0).

have a lifetime as LRDs, after which LRDs will not be observed as LRDs anymore. Following the recently proposed BH envelope model by D. Kido et al. (2025), we assume that an LRD lifetime corresponds to a Salpeter time (E. E. Salpeter 1964), which is the e-folding timescale for M_{BH} evolution with the Eddington ratio of unity:

$$\tau_{Sal}(\varepsilon) \simeq 4.5 \times 10^7 \left(\frac{\varepsilon}{0.1}\right) \text{yr,} \qquad (12)$$

where ε is the radiative efficiency. With these assumptions, the number of LRDs (n_{LRD}) and galaxies (n_{gal}) at cosmic age t_{Univ} evolve as:

$$n_{LRD}(t_{Univ}) = \tau_{Sal}(\varepsilon) \times \dot{n}_{LRD},$$
$$n_{gal}(t_{Univ}) = t_{Univ} \times \dot{n}_{gal}.$$

Thus, the expected LRD fraction is:

$$f_{LRD}(t_{Univ}) = \frac{n_{LRD}(t_{Univ})}{n_{gal}(t_{Univ})} = C \frac{\tau_{sal}(\varepsilon = 0.1)}{t_{Univ}}, \qquad (13)$$

where C is a constant:

$$C = \frac{\dot{n}_{LRD}}{\dot{n}_{gal}} \left(\frac{\varepsilon}{0.1}\right), \qquad (14)$$

including the formation rate ratio $\dot{n}_{LRD}/\dot{n}_{gal}$, uncertainty of the radiation efficiency ε, and possible deviation of the exact LRD lifetime from τ_{Sal}. This model indicates that f_{LRD} evolves as the inverse of the cosmic age, i.e., $f_{LRD} \propto t_{Univ}^{-1}$. Assuming $\varepsilon = 0.1$ (i.e., $\tau_{Sal} = 4.5 \times 10^7$ yr), the model expectation with $C = 0.3$ (blue dashed curve in Figure 8) is broadly consistent with the observed evolution of f_{LRD} at $z \gtrsim 5$. However, at $z \lesssim 3$, the observed f_{LRD} significantly declines relative to the expectation. One possible interpretation of this discrepancy is that the formation rate of LRDs decreases at $z \lesssim z_0$. $C = 0.3$ may suggest that the formation rate ratio $\dot{n}_{LRD}/\dot{n}_{gal}$ is 0.3 under the assumption of a radiation efficiency of $\varepsilon = 0.1$. However, LRDs may have higher radiation efficiencies of $\varepsilon \sim 0.3$, as suggested by K. Inayoshi & K. Ichikawa (2024); therefore, no definitive conclusion can be drawn.

As an alternative theoretical framework, we also compared the results with the model of F. Pacucci & A. Loeb (2025), in which LRDs are described as descendants of low-spin dark matter halos. The predicted evolution of f_{LRD} at $M_{UV} = -20$ (blue dotted curve in Figure 8) agrees with previous observations within the uncertainties. At $z = 10$, the model prediction is higher than our f_{LRD} measurement, but still consistent within the uncertainty. According to this model, f_{LRD} at $M_{UV} = -20$

would reach ~ 0.1 by $z = 12$. Again, our result has a large uncertainty, and it is still difficult to test and constrain the theoretical models strongly; therefore, we need to identify more LRD samples at $z \gtrsim 10$.

6.2.2. Empirical Interpretation

Following the definition of f_{LRD} (Equation 11), we also model the redshift evolution of f_{LRD} by dividing the log-normal distribution of LRDs by the evolution of the number density of the galaxy population. For the LRDs, we assume the log-normal distribution fitted to the observational results in Section 6.1 (the model shown in Figure 7). For the galaxy population, we use the evolution of the high-z UV luminosity function from R. J. Bouwens et al. (2021) and M. Franco et al. (2025b). These works first model the galaxy UV luminosity function using the Schechter function (P. Schechter 1976):

$$\Phi_{\mathrm{galaxy}}(M_{\mathrm{UV}}) = \frac{\ln 10}{2.5} \Phi^*_{\mathrm{galaxy}} 10^{-0.4(M_{\mathrm{UV}} - M^*_{\mathrm{UV}})(\alpha+1)}$$
$$\times \exp\left[-10^{-0.4(M_{\mathrm{UV}} - M^*_{\mathrm{UV}})}\right] \quad (15)$$

and provide the redshift evolution of the fitted parameters: $\Phi^*_{\mathrm{galaxy}}(z)$ (the normalization), $M^*_{\mathrm{UV}}(z)$ (the characteristic luminosity), $\alpha(z)$ (the faint-end slope). Using these parameters, we derive the galaxy number density at $M_{\mathrm{UV}} = -20$ at each redshift, and compare it with the log-normal LRD distribution to investigate the redshift evolution of f_{LRD}.

In R. J. Bouwens et al. (2021), the evolution of the scaling ($\log \Phi^*_{\mathrm{galaxy}}$) of the galaxy luminosity function is modeled by a quadratic function of z, leading to a rapid decline in the number of galaxies at $z > 10$. As a result, the model with R. J. Bouwens et al. (2021) predicts a sharp increase in the LRD fraction. On the other hand, M. Franco et al. (2025b) compiled JWST results and fitted $\log \Phi^*_{\mathrm{galaxy}}$ with a linear function of z. This yields a less extreme evolution and more consistent results with observed trends than the model with R. J. Bouwens et al. (2021). Even under the model with M. Franco et al. (2025b), the LRD fraction does not decrease beyond z_0 (the peak redshift of the log-normal distribution and $=5.8$), providing a better match to the LRD fraction at $z \sim 10$. At $z \gtrsim 16$, the model with M. Franco et al. (2025b) indicates that M^*_{UV} becomes larger than -20, resulting in a rapid decrease of the number density of galaxies at $M_{\mathrm{UV}} = -20$ and, consequently, a significant increase in the LRD fraction. This increasing trend may suggest that SMBHs become luminous more rapidly than galaxies. K. Inayoshi (2025) hypothesized that LRDs represent the first or second accretion phase following seed black hole formation. If this is the case, LRDs with $M_{\mathrm{UV}} = -20$ could emerge shortly after the seed BH formation.

As an extreme scenario, if we extrapolate the linear fit, log-normal + R. J. Bouwens et al. (2021), and log-normal + M. Franco et al. (2025b) models, each predicts that $f_{\mathrm{LRD}} > 1$ at $z > 24.0$, 13.5, and 22.7, respectively. If this scenario proves to be correct, it would suggest that the first $M_{\mathrm{UV}} = -20$ objects in the Universe were LRDs. Furthermore, these redshifts are consistent with theoretical predictions for the epoch of seed black hole formation.

These predictions are based on extrapolations from a log-normal distribution fitted to the number density derived from our candidate without spectroscopic confirmation, combined with the galaxy luminosity function. Thus, it is premature to draw firm conclusions given the significant uncertainties. As this analysis is based on comparing the single luminosity bin of $M_{\mathrm{UV}} = -20$ and a single object, larger samples across a broader luminosity range will be necessary to robustly assess the LRD fraction across cosmic time. Also, more importantly, it remains unclear whether the UV emission of LRDs originates from radiation associated with their SMBHs. Therefore, the observed UV luminosity function may not directly trace the evolution of SMBHs.

6.3. Bolometric Luminosity of CW-LRD-z10

We estimate the bolometric luminosity (L_{bol}) of CW-LRD-z10. To infer L_{bol}, we must make assumptions about the nature of the V-shaped SED and the SEDs in the MIR and longer wavelengths in which LRDs are typically undetected. Initially, the red color observed in LRDs has been interpreted as originating from dust-obscured AGNs or galaxies (e.g., H. B. Akins et al. 2023; G. Barro et al. 2024a; I. Labbe et al. 2025). However, ALMA and JWST/MIRI observations have reported that LRDs lack hot torus emission and cold dust components, suggesting that LRDs would have low-level dust attenuation (e.g., C. M. Casey et al. 2025; K. Chen et al. 2025; D. J. Setton et al. 2025). In this case, the V-shaped SED is interpreted as the intrinsic SED of the LRDs without strong dust obscuration. Additionally, strong Balmer breaks that a part of LRDs show (I. Labbe et al. 2024; C. C. Williams et al. 2024; A. de Graaff et al. 2025; X. Ji et al. 2025b; R. P. Naidu et al. 2025a) are not attributed to a stellar origin but to dense gaseous absorbers or envelopes with a high hydrogen column density of $\gtrsim$ a few 10^{23} cm^{-2} (K. Inayoshi & R. Maiolino 2025; X. Ji et al. 2025b). This supports the interpretation that the red continuum is instead associated with radiation from an accreting BH.

In this study, we conservatively assume the lower limit of the L_{bol} of CW-LRD-z10 by assuming a dust-free case (no dust attenuation and re-emission). We also adopt the interpretation suggested by recent studies that the blue excess originates from the host galaxy (e.g., D. Kido et al. 2025; R. P. Naidu et al. 2025a); thus, we assume that the UV part does not contribute to the bolometric luminosity. To estimate the intrinsic bolometric luminosity, we fit the red part of the SED (F356W, F444W, and F770W) with a blackbody spectrum assuming $T = 5000$ K and $A_V = 0$ (K. Inayoshi et al. 2025; D. Kido et al. 2025; H. Liu et al. 2025; X. Lin et al. 2025b). From the fitted results, the bolometric luminosity is estimated as $L_{\mathrm{bol}} = (2.9 \pm 0.2) \times 10^{44}$ erg s^{-1}. With the L_{bol} and λ_{Edd}, we estimate the M_{BH} as

$$\left(\frac{M_{\mathrm{BH}}}{M_\odot}\right) = \left(\frac{L_{\mathrm{bol}}}{1.26 \times 10^{38} \text{ erg s}^{-1}}\right)\left(\frac{\lambda_{\mathrm{Edd}}}{1.0}\right)^{-1}. \quad (16)$$

While we do not know the exact λ_{Edd}, we first assume an Eddington limit of $\lambda_{\mathrm{Edd}} < 1$ and obtain a lower bound $M_{\mathrm{BH}} \gtrsim 2 \times 10^6 M_\odot$. Thus, we may be witnessing an SMBH with mass slightly higher than that expected for the heavy-seed scenario with direct-collapse BHs, $M_{\mathrm{BH}} \lesssim 10^6 M_\odot$. The number density of $10^6 M_\odot$ SMBHs at $z \sim 10$ is predicted to be around 10^{-6} Mpc^{-3} dex^{-1} in the BH mass function (W. Li et al. 2024), which is roughly consistent with our UV luminosity function. If, however, LRDs are accreting at super-Eddington rates as proposed in some studies (K. Inayoshi et al. 2024;

E. Lambrides et al. 2024; P. Madau & F. Haardt 2024; F. Pacucci & R. Narayan 2024; H. Liu et al. 2025), the actual black hole mass could be significantly lower; the BH mass would decrease to $2 \times 10^5 M_\odot$ with $\lambda_{\rm Edd} = 10$. Such BH masses of $\lesssim 10^6 M_\odot$ may be consistent with the scenario proposed by K. Inayoshi (2025), in which LRDs are in the phase shortly after the formation of heavy-seed black holes, which are typically predicted to have masses of $10^{5-6} M_\odot$.

Nevertheless, this BH mass estimation carries substantial uncertainties, as it relies on various assumptions, including the shape of the SED and the Eddington ratio. Since bright Balmer lines such as Hα and Hβ fall outside of the wavelength coverage of NIRSpec at $z \sim 10$, deep spectroscopic follow-up with MIRI will be essential to obtain more robust constraints on $M_{\rm BH}$.

6.4. Prospects

Because NIRSpec only covers wavelengths up to the rest-frame $<0.5\,\mu$m at $z \sim 10$, deep spectroscopic follow-up observation with MIRI is essential for a robust confirmation of the redshift and physical nature of this candidate. To reduce the uncertainty of the luminosity function (and LRD fraction) and enable the derivation of the luminosity function shape across different magnitude bins, we need to increase the sample size and expand the luminosity range of the sample. One straightforward way to do this is to expand NIRCam-MIRI joint surveys in both area and depth. F560W photometry can effectively help distinguish $z \sim 10$ LRDs from the $z \sim 0.2$ solution; therefore, increasing the number of MIRI filters in future surveys is helpful to robustly select LRD candidates. Given the rarity of $z \gtrsim 10$ galaxies, another efficient strategy to search for $z \gtrsim 10$ LRDs is MIRI follow-up of $z \gtrsim 10$ galaxy candidates found in NIRCam surveys. To further improve the robustness of the selection and completeness estimates, it will also be important to construct an SED template that incorporates the diversity of LRDs' SEDs, based on archival LRD spectra and upcoming spectroscopic data from ongoing spectroscopic campaigns such as EMBER (GO 7076,[77] PI: H. B. Akins).

Furthermore, a future survey project with the Galaxy Reionization EXplorer and PLanetary Universe Spectrometer (GREX-PLUS; GREX-PLUS Science Team et al. 2023; A. K. Inoue et al. 2024), a 1.0 m infrared space telescope for the 2030s, is expected to increase the sample size of bright high-z LRDs. The Deep survey of its wide-field camera with five filters covering 2–8 μm will cover an area of 10 deg^2 with 5σ limiting magnitudes of 26.5–23.5 mag (A. K. Inoue et al. 2024). Combined with near-infrared deep survey data from Euclid or Roman, this survey will be capable of detecting LRDs with $M_{\rm UV} \lesssim -21.5$ and $\lesssim -22.5$ at $z \sim 10$ and $z \sim 13$, respectively, making it a valuable tool for exploring bright LRDs at $z \lesssim 13$. At $z > 15$, the wide-field camera only covers the rest-frame $\lesssim 0.5\,\mu$m, making it difficult to distinguish LRDs from galaxies with strong emission lines or prominent Balmer breaks, similar to the limitations of NIRCam-only selections for $z \sim 10$ LRDs (Section 1 and Appendix A). Therefore, complementary observations with MIRI covering $>8\,\mu$m will be crucial. Bright galaxy candidates at $z \gtrsim 15$ identified by GREX-PLUS (Y. Harikane et al. 2022b, 2025)

---

[77] www.stsci.edu/jwst/science-execution/program-information?id=7076

should be followed up with MIRI, enabling the exploration of LRDs at even higher redshifts.

7. Conclusion

We conduct a joint color selection using both NIRCam and MIRI data to push the study of LRDs to $z \gtrsim 10$. The combination of NIRCam and MIRI enables the selection of LRD candidates at $z \sim 10$, a redshift range that has been difficult to probe using previous NIRCam-only selection methods. We demonstrate that the color–color diagram using F277W, F444W, and F770W (Figure 2, right panel) can efficiently separate $z \sim 10$ LRDs from contaminants. The key results are as follows:

1. By applying the selection with S/N (an F115W-dropout condition), colors (Equations (1), (2), and (3)), and compactness, we identify one robust $z \sim 10$ LRD candidate, CW-LRD-z10, from the 0.18 deg^2 of the NIRCam-MIRI overlap region in COSMOS-Web. CW-LRD-z10 exhibits a clear V-shaped SED (Section 5.1), an F115W dropout, and a compact morphology consistent with a point source (Section 5.2).

2. A possible contaminant showing colors similar to those of $z \sim 10$ LRDs is a dusty SFG at $z \sim 0.2$, where PAH 3.3 μm and 5.6 μm features can boost the F444W and F770W fluxes. However, our SED fitting (Section 5.3) and morphological analysis (Section 5.2) strongly support the $z \sim 10$ LRD interpretation. In particular, the nondetections in F814W, F115W, and F1000W are inconsistent with the $z \sim 0.2$ dusty SFG case (Figure 4).

3. The observed red color from F356W to F770W cannot be reproduced by $z \sim 10$ non-LRD galaxies with strong emission lines or stellar-origin Balmer breaks. To reproduce this color, not only is a strong Hα line but also a steep red continuum slope, characteristic of LRDs, required (Section 5.1). Therefore, we conclude that CW-LRD-z10 is highly likely to be an LRD at $z_{\rm photo} = 10.50^{+0.72}_{-0.58}$ with the UV absolute magnitude of $M_{\rm UV} = -19.9^{+0.1}_{-0.2}$.

4. Assuming CW-LRD-z10 is a genuine $z \sim 10$ LRD, we derive the luminosity function of $z \sim 10$ LRD at $M_{\rm UV} = -20$ in Section 6.1 (Figure 6) as $\Phi_{\rm LRD}(M_{\rm UV} = -20) = (1.2^{+2.7}_{-1.0}) \times 10^{-6}$ Mpc^{-3} mag^{-1}, consistent with a decline toward the highest redshifts from a peak at $z \sim 6$ (Section 6.1, Figure 7).

5. The fraction of LRDs among the overall galaxy population with $M_{\rm UV} = -20$ reaches $2.6^{+5.9}_{-2.1}\%$ at $z \sim 10$, intriguingly suggesting that an even higher LRD fraction may be expected at $z > 10$ (Section 6.2). In an extreme scenario, extrapolating the evolution of the LRD fraction based on the number density evolution of both LRDs and galaxies indicates that the LRD fraction could approach ~ 1 at $z \sim 20$–30 (Figure 8). If this is the case, it may imply that SMBHs can become luminous more rapidly than galaxies, and that the very first $M_{\rm UV} = -20$ sources in the Universe may have been LRDs.

6. Under the assumption of a blackbody SED with no dust attenuation and an Eddington-limited accretion, we estimate the BH mass to be $M_{\rm BH} \gtrsim 10^6 M_\odot$, placing this object among the most distant known active SMBHs and possibly witnessing the initial accretion phase of a seed

black hole, as suggested in K. Inayoshi (2025; see also Section 6.3).

Follow-up MIRI spectroscopy is essential to confirm the redshift, verify the nature of the source as an LRD, and better constrain the BH mass. In the future, expanding MIRI surveys in terms of survey field and the number of filters, along with next-generation missions such as GREX-PLUS (GREX-PLUS Science Team et al. 2023; A. K. Inoue et al. 2024), which will explore much wider areas than JWST in the 2–8 μm range, will be crucial to increasing the sample of $z \gtrsim 10$ LRDs. These efforts will enable improved statistics and a more comprehensive sample over a broader luminosity range, providing key insights into the formation of SMBHs in the early Universe.

Appendix A
High-redshift LRDs in D. D. Kocevski et al. (2024)

D. D. Kocevski et al. (2025) selected LRD candidates at $2 < z_{\rm photo} < 11$ based on the slope of the SED using only NIRCam photometry. Among them, 13 objects listed in Table 4 have the best-fit photometric redshift of $z_{\rm photo} \geqslant 10$ in D. D. Kocevski et al. (2025). We examine archival JWST spectroscopic data and find that archival spectra already exist for six out of the 13 candidates from GTO 1287[78] (PI: K. Isaak), GO 4233[79] (see footnote 71; RUBIES, PI: A. de Graaff and G. Brammer), and GO 6368[80] (CAPERS, PI: M. Dickinson). While we do not provide a detailed analysis for each object here, as it is beyond the scope of this paper, we perform a quick look at processed data in the Mikulski Archive for Space Telescopes (MAST[81]) and the DJA, and manually estimate $z_{\rm spec}$. The confirmed $z_{\rm spec}$ is summarized in Table 4. Three of them have $z_{\rm spec} < 9$ (5.93, 6.07, and 8.50), and the three are at $9 < z_{\rm spec} < 10$ (9.29, 9.65, and 9.94). Thus, simply using these numbers, the success rate for a genuine $z_{\rm spec} \sim 10$ object in the $z_{\rm photo} > 10$ sample in D. D. Kocevski et al. (2025) is 50%.

Among the three $9 < z_{\rm spec} < 10$ objects, one is CAPERS-LRD-z9 spectroscopically confirmed as an LRD in A. J. Taylor et al. (2025b). Then, one is CEERS-23931 at $z_{\rm spec} = 9.94$ already reported as CAPERS-EGS-25297 in C. L. Pollock et al. (2025) and C. T. Donnan et al. (2025). CEERS-23931 has an optical continuum slope of $\beta = -0.65$ ($f_\lambda \propto \lambda^\beta$, C. T. Donnan et al. 2025), not spectroscopically showing a sign of the steep red continuum. Instead, this object has extremely strong emission lines, such as [O II] $\lambda\lambda3726,3729$, [Ne III]$\lambda3869$, [Ne III]$\lambda3967$+Hϵ, Hδ, and Hγ +[O III]$\lambda4363$, and these strong emission lines boosts the F410M and F444W photometry and mimic the V-shaped color in NIRCam photometry (see C. T. Donnan et al. 2025).

The other object is JADES-67592 at $z_{\rm spec} = 9.65$ with $M_{\rm UV} = -17.12$. Due to the faintness, it is challenging to confirm the presence of a broad Hβ line (Figure 9). JADES-67592 spectroscopically exhibits a Balmer break, as shown in Figure 9, and the strength of the Balmer break, defined as an f_ν ratio between the rest-frame wavelength ranges of 3620–3720 Å and 4000–4100 Å, is $\sim$2. This break strength can be reproduced by a stellar-origin Balmer break. JADES-67592 is not detected in either F560W or F770W from SMILES (GTO 1207,[82] (see footnote 65) PI: G. Rieke; G. H. Rieke et al. 2024) due to its faint nature ($M_{\rm UV} = -17.5$). Given the 5σ detection limits for a point source of SMILES, $f_{\rm F560W} = 0.21\,\mu$Jy and $f_{\rm F770W} = 0.20\,\mu$Jy (S. Alberts et al. 2024), the color upper limit of


Table 4
$z_{\text{photo}} > 10$ Candidates Reported in D. D. Kocevski et al. (2025)

ID	R.A. (deg)	Decl. (deg)	M_{UV}	z_{photo}	z_{spec}	PID	Comments
CEERS-23931	214.817112	52.748343	−19.77	10.21	9.94	6368	Non-LRD, EGS-25297 (C. T. Donnan et al. 2025)
JADES-67592	53.072478	−27.855352	−17.12	11.26	9.65	1287	Not detected in F560W and F770W
JADES-82209	53.197512	−27.782456	−18.05	10.48	⋯	⋯	Detected in F115W
PRIMER-COS-46911	150.175418	2.234439	−18.84	10.60	⋯	⋯	⋯
PRIMER-COS-70533	150.136254	2.30803	−18.11	11.92	9.29	6368	CAPERS-LRD-z9 (A. J. Taylor et al. 2025b)
PRIMER-COS-78729	150.161027	2.465804	−19.02	10.45	5.93	6368	Detected in F090W and F115W
PRIMER-COS-113415	150.155705	2.33761	−17.58	10.69	⋯	⋯	Not detected in F770W
PRIMER-UDS-66751	34.254151	−5.290015	−18.28	10.54	6.07	4233	tentatively detected in F115W
PRIMER-UDS-106389	34.426489	−5.225494	−19.29	11.29	⋯	⋯	Not covered with F770W
PRIMER-UDS-134793	34.505257	−5.176794	−18.01	10.57	⋯	⋯	Not covered with F770W
PRIMER-UDS-151408	34.404447	−5.104179	−18.91	11.38	⋯	⋯	Not covered with F770W
PRIMER-UDS-151980	34.422908	−5.104757	−18.80	10.48	⋯	⋯	Not detected in F770W
PRIMER-UDS-173887	34.238463	−5.140396	−18.81	10.00	8.50	4233	Detected in F770W

Note. ID, R.A., decl., M_{UV}, and z_{photo} are from Table 3 in D. D. Kocevski et al. (2025). Note that, for objects with available z_{spec}, we update M_{UV} with the value calculated with m_{UV}, β_{UV}, z_{photo}, and z_{spec}.
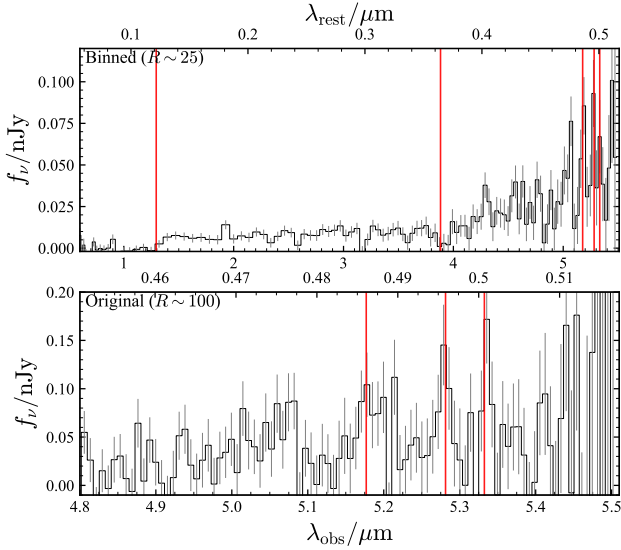
Figure 9. Spectrum of JADES-67592 ($z_{\text{spec}} = 9.65$) downloaded from DJA. The upper and lower panels show the overall four-times binned PRISM spectra ($R \sim 25$) and the zoomed-in original ($R \sim 100$) spectra around $H\beta$ + [O III]$\lambda\lambda$4959, 5007. The wavelengths of Lyα, Balmer limit, Hβ, and [O III]$\lambda\lambda$4959, 5007 are shown in red vertical lines.

$m_{\text{F444W}} - m_{\text{F770W}} < 3$ is not stringent enough to robustly distinguish between a Balmer break galaxy and an LRD at $z \sim 10$ (see Figure 2). Thus, with the currently available data, we cannot confirm if JADES-67592 is a genuine LRD or not. To confirm the nature, deep MIRI photometry is needed to distinguish between an LRD and a galaxy with a stellar-origin Balmer break. It is also important to obtain a deeper NIRSpec spectrum to confirm the presence of a broad Hβ line.

These results indicate that, without incorporating MIRI F770W data, there is a risk of selecting contaminant sources that are not genuine $z \sim 10$ LRDs, highlighting the advantage of our NIRCam-MIRI joint selection method in reliably identifying $z \sim 10$ LRDs. Also note that all of the spectroscopically unconfirmed $z_{\text{photo}} > 10$ LRD candidates in

D. D. Kocevski et al. (2025) have $M_{\text{UV}} \gtrsim -19$. Thus, our candidate, CW-LRD-z10, with $M_{\text{UV}} = -19.9$, discovered in a relatively shallow but wide-area field, complements their candidates by probing the brighter end of the LRD population.

Appendix B
Objects Excluded in the Visual Inspection

As described in Section 3.2 and summarized in Table 1, five objects that pass the selection criteria based on S/N, color, and compactness are excluded through visual inspection, and only CW-LRD-z10 is selected as a final candidate. In this appendix, we show images of the five excluded objects listed in Table 5 to demonstrate why they are unlikely to be $z \sim 10$ LRDs. Figure 10 shows cutout images of these sources (and CW-LRD-z10 for comparison) normalized by the noise map. These objects are generally excluded because they are not clearly detected in the F770W band. Their F770W images are indistinguishable from the surrounding noise, suggesting that their F770W photometry may have been strongly influenced by noise. Indeed, in COSMOS2025, the F770W signal-to-noise ratios (S/N$_{\text{F770W}}$) for all objects except CW-LRD-z10 (ID: 426069) are $\lesssim 10$, significantly lower S/N values compared to CW-LRD-z10.

Also note that some galaxy candidates are detected in HSC or F115W when combining all available JWST imaging data (i.e., not limited to COSMOS-Web alone). ID: 71585 is detected in HSC and F115W, and ID: 657448 is detected in F090W and F115W from the combined PRIMER and COSMOS-Web data, suggesting that these are likely low-redshift interlopers. If all four remaining candidates are $z \sim 10$ LRDs, the number density with $M_{\text{UV}} = -20$ estimated in Section 6.1 would increase to $\Phi_{\text{LRD}} = (4.7^{+3.7}_{-2.2}) \times 10^{-6}$ Mpc^{-3} mag^{-1}. Correspondingly, the LRD fraction at $z \sim 10$ calculated in Section 6.2 would increase to $f_{\text{LRD}, M_{\text{UV}} = -20} = 9.9^{+7.8}_{-4.7}\%$. However, given that their appearance is indistinguishable from noise in the F770W image, it is unlikely that these F770W detections are real. Future spectroscopic confirmation will be essential to verify whether these candidates are indeed not $z \sim 10$ LRDs.
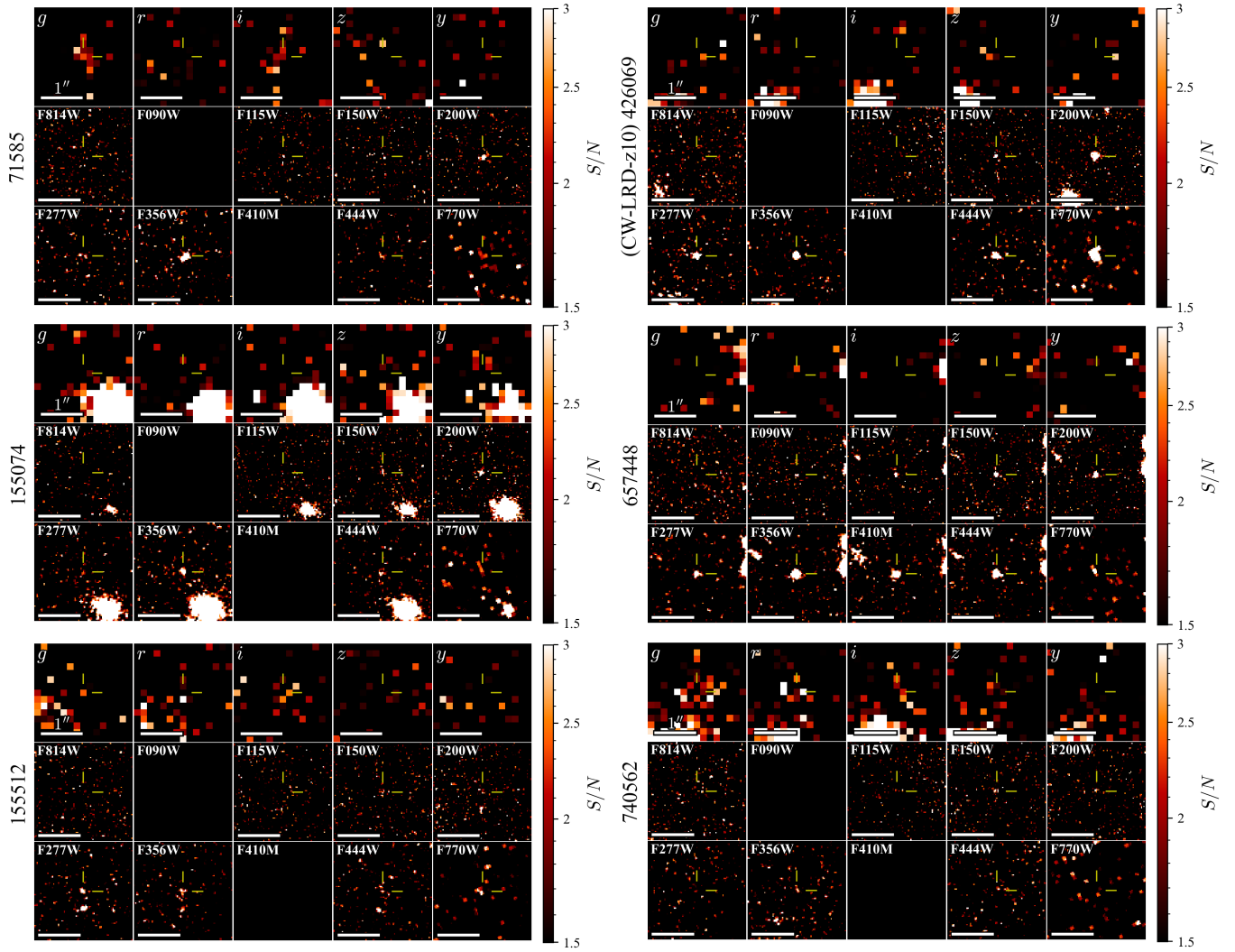
Figure 10. HSC (*grizy*), HST (F814W), and JWST $2''5 \times 2''5$ cutout images centered on each object excluded in visual inspection. For comparison, we also plot CW-LRD-z10 (`ID:426069`). Each image is scaled by a noise map.

Table 5
Objects Excluded in Visual Inspection Process

| ID	R.A. (deg)	Decl. (deg)	z_{photo}	S/N$_{F770W}$	M_{UV}	Comments
71585	149.9223103	2.166595859	$0.23^{+0.10}_{-0.08}$	11.0	−19.8	Detected in HSC *g*
155074	150.2131795	2.133412186	$9.3^{+0.7}_{-1.1}$	9.8	−20.3	Not clearly detected in F770W
155512	150.2246714	2.137034303	$0.12^{+0.05}_{-0.07}$	12.4	−19.5	Not clearly detected in F150W, F444W, and F770W
426069	150.0841004	2.453894622	$0.17^{+0.01}_{-0.01}$	31.6	−19.9	Reported as CW-LRD-z10
657448	150.0995828	2.337128099	$8.5^{+0.3}_{-0.7}$	7.9	−19.2	Detected in F115W (PRIMER)
740562	150.2236736	2.223625423	$0.2^{+2.0}_{-0.2}$	6.0	−20.3	Not clearly detected in F770W

Note. ID, R.A., decl., z_{photo}, and S/N$_{F770W}$ are from COSMOS2025 catalog (M. Shuntov et al. 2025). M_{UV} is calculated from F150W photometry and the assumption of $z = 10$.

Appendix C
Flux–FWHM Relationship Suggesting a Compact Morphology

To confirm the compact morphology independently of the image-based fitting (Section 4.3), we examine the relationship between flux and FWHM for objects within the F200W image from COSMOS-3D, where CW-LRD-z10 is detected with the highest S/N among all filters due to its relatively long exposure time. The flux is approximately measured using `DAOStarFinder` in `photutils`, which is based on based on the DAOFIND algorithm (P. B. Stetson 1987). We set the FWHM of a 2D Gaussian kernel (`fwhm` parameter in `DAOStarFinder`) to 4 pixels. For each source detected by `DAOStarFinder`, we measure FWHM using the `measure_`
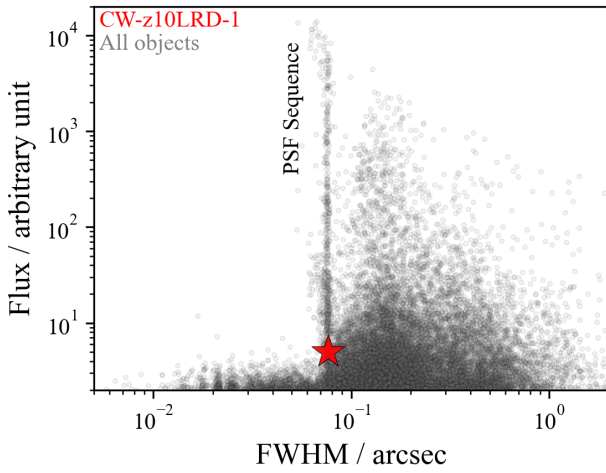
Figure 11. Flux as a function of FWHM for all detected objects in a single tile of the F200W image ($\sim 0.019\,\mathrm{deg}^2$), measured using measure_FWHM function in galight. CW-LRD-z10 exhibits an FWHM consistent with the sequence of point sources, strongly suggesting that it is a very compact object similar to previously found LRDs.

FWHM function in galight. Figure 11 shows that CW-LRD-z10 exhibits an FWHM consistent with the sequence of objects following point sources. This result supports that a point source well describes the morphology of CW-LRD-z10, as suggested from the image-based morphological fitting (Section 5.2).

Appendix D
SED Fitting with EAZY

Generally, the results of SED fitting analyses depend on the choice of templates or models (e.g., S. Wuyts et al. 2009; S. L. Newman et al. 2025). To minimize dependencies on a specific method, we also utilize EAZY (G. B. Brammer et al. 2008), a widely used code for estimating photometric redshifts by fitting observed data with template libraries. In this study, we apply the following three fitting setups using public templates:
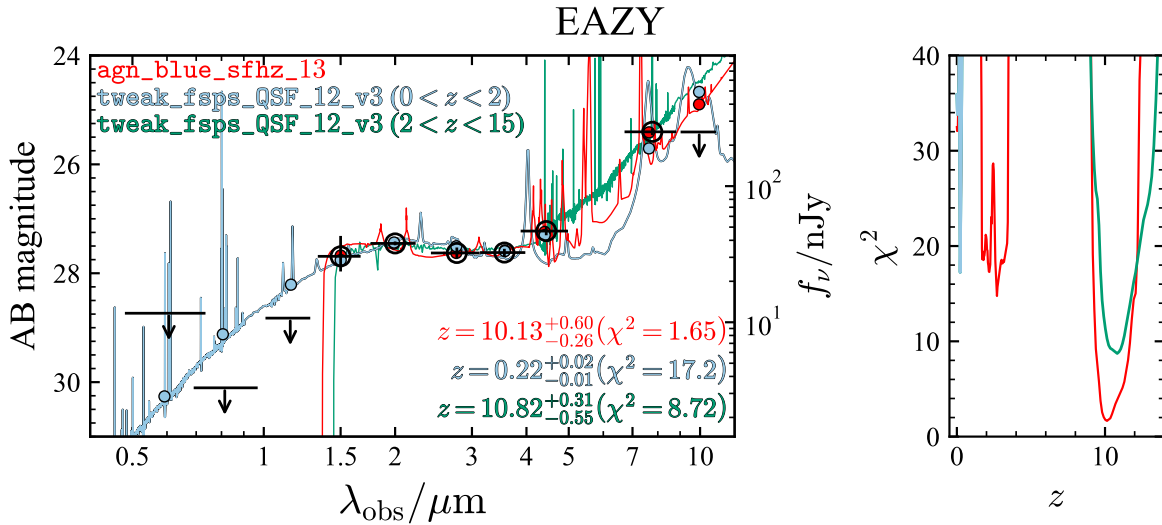
1. Fitting with a sorted_agn_blue_sfhz_13 template set, a template set for LRDs constructed based on the spectrum in M. Killi et al. (2024) and available in EAZY, using a redshift range of $z = 0$–15 with a step of $\Delta z = 0.01$.
2. Fitting with a galaxy template set, tweak_fsps_QSF_12_v3, using a redshift range of $z = 2$–15 with a step of $\Delta z = 0.01$ for specifically testing the high-z non-LRD galaxy case.
3. Fitting with a galaxy template set, tweak_fsps_QSF_12_v3, using a redshift range of $z = 0$–2 with a step of $\Delta z = 0.01$ for specifically testing the $z \sim 0.2$ interloper case.

One huge difference between EAZY and BAGPIPES (Section 4.2) is that BAGPIPES assumes a single galaxy population, in contrast to EAZY, which fits composite SEDs from multiple templates. The χ^2 distribution and the best-fit model SED are shown in Figure 12.

When fitting over the wide redshift range of $0 < z < 15$ with the sorted_agn_blue_sfhz_13 (LRD) template set, we obtain a best-fit photometric redshift of $z_{\mathrm{photo}} = 10.13^{+0.60}_{-0.26}$. Then, when fitting over the low-redshift range of $0 < z < 2$ with tweak_fsps_QSF_12_v3 (galaxy) template, we obtain a best-fit photometric redshift of $z_{\mathrm{photo}} = 0.22^{+0.02}_{-0.01}$. Thus, the $z \sim 10$ LRD solution has much lower χ^2 with $\Delta\chi^2 = 15.6$ than the $z \sim 0.2$ galaxy case, consistent with the results with BAGPIPES (Section 5.3). Also note that the inferred photometric redshift with the LRD template ($z_{\mathrm{photo}} = 10.13^{+0.60}_{-0.26}$) is consistent with the result obtained using the H. B. Akins et al. (2024) model ($z_{\mathrm{photo}} = 10.50^{+0.72}_{-0.58}$) within the 1σ confidence level.

Fitting over the high-redshift range of $2 < z < 15$ with the tweak_fsps_QSF_12_v3 (galaxy) template yields a photometric redshift of $z_{\mathrm{photo}} = 10.82^{+0.31}_{-0.55}$. The $z \sim 10$ galaxy fitting has a higher χ^2 value, with $\Delta\chi^2 = 7.07$, compared to the $z \sim 10$ LRD solution. A major difference from the BAGPIPES results is that, with EAZY, the $z \sim 10$ galaxy case can simultaneously reproduce both the rest-frame UV and rest-frame optical parts of the SED, resulting in a lower χ^2 than the $z \sim 10$ galaxy model fit obtained with BAGPIPES (Figure 4 green line). This improved fitting result arises because EAZY models SEDs as a linear combination of multiple templates, each potentially characterized by different physical parameters. In this case, the best-fit SED consists of a combination of a dust-unobscured SFG ($A_V = 0.068$, $M_* = 2.5 \times 10^{10} M_\odot$, and SFR $= 4.8 M_\odot\,\mathrm{yr}^{-1}$) and a dust-obscured massive quiescent galaxy ($A_V = 2.884$, $M_* = 6.2 \times 10^{11} M_\odot$, and SFR $\simeq 0 M_\odot\,\mathrm{yr}^{-1}$), each contributing primarily to the rest-frame UV and rest-frame optical parts of the SED, respectively. Notably, the total inferred stellar mass ($M_* = 6.5 \times 10^{11} M_\odot$) is too large for a galaxy at $z \sim 10$ and is not allowed in the framework of the ΛCDM, even assuming a global star formation efficiency of $\epsilon = 1$ (M. Boylan-Kolchin 2023). Furthermore, when combined with the upper limit on the galaxy size ($<120\,\mathrm{pc}$; Section 5.2), the inferred M_* implies a lower limit on the stellar mass density of $\Sigma_* > 7.2 \times 10^{12} M_\odot\,\mathrm{kpc}^{-2}$. This value far exceeds the maximum surface densities observed in compact stellar systems in the local Universe ($\Sigma_* \sim 3 \times 10^{11} M_\odot\,\mathrm{kpc}^{-2}$; P. F. Hopkins et al. 2010; M. Y. Grudić et al. 2019), making it physically implausible.

Thus, even based on the fitting results from EAZY, we conclude that the most plausible interpretation of CW-LRD-z10 is an LRD at $z_{\mathrm{photo}} = 10.13^{+0.60}_{-0.26}$. With this photometric redshift, the inferred UV absolute magnitude is $M_{\mathrm{UV}} = -19.9 \pm 0.1$, consistent with the result derived from the BAGPIPES fitting (Section 5.3).

Figure 12. Same as Figure 4 but for the results with EAZY. Red, cyan, and green correspond to fits using the `sorted_agn_blue_sfhz_13` template over $0 < z < 15$, the `tweak_fsps_QSF_12_v3` template over $0 < z < 2$, and the `tweak_fsps_QSF_12_v3` template over $2 < z < 15$, respectively.

ORCID iDs

Takumi S. Tanaka ⓘ https://orcid.org/0009-0003-4742-7060
Hollis B. Akins ⓘ https://orcid.org/0000-0003-3596-8794
Yuichi Harikane ⓘ https://orcid.org/0000-0002-6047-430X
John D. Silverman ⓘ https://orcid.org/0000-0002-0000-6977
Caitlin M. Casey ⓘ https://orcid.org/0000-0002-0930-6466
Kohei Inayoshi ⓘ https://orcid.org/0000-0001-9840-4959
Jan-Torge Schindler ⓘ https://orcid.org/0000-0002-4544-8242
Kazuhiro Shimasaku ⓘ https://orcid.org/0000-0002-2597-2231
Dale D. Kocevski ⓘ https://orcid.org/0000-0002-8360-3880
Masafusa Onoue ⓘ https://orcid.org/0000-0003-2984-6803
Andreas L. Faisst ⓘ https://orcid.org/0000-0002-9382-9832
Brant E. Robertson ⓘ https://orcid.org/0000-0002-4271-0364
Vasily Kokorev ⓘ https://orcid.org/0000-0002-5588-9156
Marko Shuntov ⓘ https://orcid.org/0000-0002-7087-0701
Anton M. Koekemoer ⓘ https://orcid.org/0000-0002-6610-2048
Maximilien Franco ⓘ https://orcid.org/0000-0002-3560-8599
Eiichi Egami ⓘ https://orcid.org/0000-0003-1344-9475
Daizhong Liu ⓘ https://orcid.org/0000-0001-9773-7479
Anthony J. Taylor ⓘ https://orcid.org/0000-0003-1282-7454
Jeyhan S. Kartaltepe ⓘ https://orcid.org/0000-0001-9187-3605
Sarah E. I. Bosman ⓘ https://orcid.org/0000-0001-8582-7012
Jaclyn B. Champagne ⓘ https://orcid.org/0000-0002-6184-9097
Koki Kakiichi ⓘ https://orcid.org/0000-0001-6874-1321
Santosh Harish ⓘ https://orcid.org/0000-0003-0129-2079
Zijian Zhang ⓘ https://orcid.org/0000-0002-2420-5022
Sophie L. Newman ⓘ https://orcid.org/0009-0001-3422-3048
Darshan Kakkad ⓘ https://orcid.org/0000-0002-2603-2639
Qinyue Fei ⓘ https://orcid.org/0000-0001-7232-5355
Seiji Fujimoto ⓘ https://orcid.org/0000-0001-7201-5066
Mingyu Li ⓘ https://orcid.org/0000-0001-6251-649X
Steven L. Finkelstein ⓘ https://orcid.org/0000-0001-8519-1130
Zi-Jian Li ⓘ https://orcid.org/0000-0001-7634-1547
Erini Lambrides ⓘ https://orcid.org/0000-0003-3216-7190
Laura Sommovigo ⓘ https://orcid.org/0000-0002-2906-2200
Jorge A. Zavala ⓘ https://orcid.org/0000-0002-7051-1100
Kei Ito ⓘ https://orcid.org/0000-0002-9453-0381
Zhaoxuan Liu ⓘ https://orcid.org/0000-0002-9252-114X
Ezequiel Treister ⓘ https://orcid.org/0000-0001-7568-6412
Manuel Aravena ⓘ https://orcid.org/0000-0002-6290-3198
Ghassem Gozaliasl ⓘ https://orcid.org/0000-0002-0236-919X
Haowen Zhang ⓘ https://orcid.org/0000-0002-4321-3538
Hossein Hatamnia ⓘ https://orcid.org/0009-0007-3673-4523
Hiroya Umeda ⓘ https://orcid.org/0009-0008-0167-5129
Akio K. Inoue ⓘ https://orcid.org/0000-0002-7779-8677
Jinyi Yang ⓘ https://orcid.org/0000-0001-5287-4242
Makoto Ando ⓘ https://orcid.org/0000-0002-4225-4477
Junya Arita ⓘ https://orcid.org/0009-0007-0864-7094
Xuheng Ding ⓘ https://orcid.org/0000-0001-8917-2148
Suin Matsui ⓘ https://orcid.org/0009-0009-7403-8603
Yuki Shibanuma ⓘ https://orcid.org/0009-0005-7449-8184
Georgios Magdis ⓘ https://orcid.org/0000-0002-4872-2294
Mingyang Zhuang ⓘ https://orcid.org/0000-0001-5105-2837
Xiaohui Fan ⓘ https://orcid.org/0000-0003-3310-0131
Zihao Li ⓘ https://orcid.org/0000-0001-5951-459X
Weizhe Liu ⓘ https://orcid.org/0000-0003-3762-7344
Jianwei Lyu ⓘ https://orcid.org/0000-0002-6221-1829
Jason Rhodes ⓘ https://orcid.org/0000-0002-4485-8549
Sune Toft ⓘ https://orcid.org/0000-0003-3631-7176
Feige Wang ⓘ https://orcid.org/0000-0002-7633-431X
Siwei Zou ⓘ https://orcid.org/0000-0002-3983-6484
Rafael C. Arango-Toro ⓘ https://orcid.org/0000-0002-0569-5222
Andrew J. Battisti ⓘ https://orcid.org/0000-0003-4569-2285
Steven Gillman ⓘ https://orcid.org/0000-0001-9885-4589
Ali Ahmad Khostovan ⓘ https://orcid.org/0000-0002-0101-336X
Arianna S. Long ⓘ https://orcid.org/0000-0002-7530-8857
Bahram Mobasher ⓘ https://orcid.org/0000-0001-5846-4404
David B. Sanders ⓘ https://orcid.org/0000-0002-1233-9998

References

Akins, H. B., Casey, C. M., Allen, N., et al. 2023, ApJ, 956, 61
Akins, H. B., Casey, C. M., Lambrides, E., et al. 2025, ApJ, 991, 37
Akiyama, M., He, W., Ikeda, H., et al. 2018, PASJ, 70, S34

Alberts, S., Lyu, J., Shivaei, I., et al. 2024, ApJ, 976, 224
Allard, F., Homeier, D., & Freytag, B. 2012, RSPTA, 370, 2765
Álvarez-Márquez, J., Crespo Gómez, A., Colina, L., et al. 2025, A&A, 695, A250
Ananna, T. T., Bogdán, Á., Kovács, O. E., Natarajan, P., & Hickox, R. C. 2024, ApJL, 969, L18
Bañados, E., Schindler, J.-T., Venemans, B. P., et al. 2023, ApJS, 265, 29
Baggen, J. F. W., van Dokkum, P., Brammer, G., et al. 2024, ApJL, 977, L13
Bagley, M. B., Finkelstein, S. L., Koekemoer, A. M., et al. 2023, ApJL, 946, L12
Barro, G., Pérez-González, P. G., Kocevski, D. D., et al. 2024a, ApJ, 963, 128
Barro, G., Perez-Gonzalez, P. G., Kocevski, D. D., et al. 2024b, arXiv:2412.01887
Bertin, E., Schefer, M., Apostolakos, N., et al. 2020, in ASP Conf. Ser. 527, Astronomical Data Analysis Software and Systems XXIX, ed. R. Pizzo et al. (San Francisco, CA: ASP), 461
Bogdán, Á., Goulding, A. D., Natarajan, P., et al. 2024, NatAs, 8, 126
Bouchet, P., García-Marín, M., Lagage, P. O., et al. 2015, PASP, 127, 612
Bouwens, R., Illingworth, G., Oesch, P., et al. 2023, MNRAS, 523, 1009
Bouwens, R. J., Oesch, P. A., Stefanon, M., et al. 2021, AJ, 162, 47
Boylan-Kolchin, M. 2023, NatAs, 7, 731
Brammer, G. 2023a, grizli, v1.9.11, Zenodo, doi:10.5281/zenodo.8370018
Brammer, G. 2023b, msaexp: NIRSpec Analyis Tools, v0.6.17, Zenodo, doi:10.5281/zenodo.8319596
Brammer, G. B., van Dokkum, P. G., & Coppi, P. 2008, ApJ, 686, 1503
Bunker, A. J., Saxena, A., Cameron, A. J., et al. 2023, A&A, 677, A88
Bushouse, H., Eisenhamer, J., Dencheva, N., et al. 2023, JWST Calibration Pipeline, v1.12.5, Zenodo, doi:0.5281/zenodo.10022973
Bushouse, H., Eisenhamer, J., Dencheva, N., et al. 2025, JWST Calibration Pipeline, v1.17.1, Zenodo, doi:0.5281/zenodo.14597407
Byler, N., Dalcanton, J. J., Conroy, C., & Johnson, B. D. 2017, ApJ, 840, 44
Carnall, A. C., McLure, R. J., Dunlop, J. S., & Davé, R. 2018, MNRAS, 480, 4379
Carniani, S., Hainline, K., D'Eugenio, F., et al. 2024, Natur, 633, 318
Casey, C. M., Akins, H. B., Finkelstein, S. L., et al. 2025, ApJL, 990, L61
Casey, C. M., Akins, H. B., Shuntov, M., et al. 2024, ApJ, 965, 98
Casey, C. M., Kartaltepe, J. S., Drakos, N. E., et al. 2023, ApJ, 954, 31
Chen, K., Li, Z., Inayoshi, K., & Ho, L. C. 2025, arXiv:2505.22600
Civano, F., Marchesi, S., Comastri, A., et al. 2016, ApJ, 819, 62
Conroy, C., & Gunn, J. E. 2010, ApJ, 712, 833
Conroy, C., Gunn, J. E., & White, M. 2009, ApJ, 699, 486
COSMOS Project 2020, Cosmic Evolution Survey with HST (COSMOS), IPAC, doi:10.26131/IRSA178
de Graaff, A., Rix, H.-W., Carniani, S., et al. 2024, A&A, 684, A87
de Graaff, A., Rix, H.-W., Naidu, R. P., et al. 2025, A&A, 701, A168
Ding, X., Silverman, J., Treu, T., et al. 2020, ApJ, 888, 37
Donnan, C. T., Dickinson, M., Taylor, A. J., et al. 2025, ApJ, 993, 224
Donnan, C. T., McLeod, D. J., Dunlop, J. S., et al. 2023, MNRAS, 518, 6011
Euclid Collaboration, Bisigello, L., Rodighiero, G., et al. 2025, arXiv:2503.15323
Fan, X., Narayanan, V. K., Lupton, R. H., et al. 2001, AJ, 122, 2833
Ferland, G. J., Chatzikos, M., Guzmán, F., et al. 2017, RMxAA, 53, 385
Ferland, G. J., Korista, K. T., Verner, D. A., et al. 1998, PASP, 110, 761
Franco, M., Akins, H. B., Casey, C. M., et al. 2024, ApJ, 973, 23
Franco, M., Casey, C. M., Akins, H. B., et al. 2025b, arXiv:2508.04791
Franco, M., Casey, C. M., Koekemoer, A. M., et al. 2025a, arXiv:2506.03256
Furtak, L. J., Labbé, I., Zitrin, A., et al. 2024, Natur, 628, 57
Furtak, L. J., Secunda, A. R., Greene, J. E., et al. 2025, A&A, 698, A227
Furtak, L. J., Zitrin, A., Plat, A., et al. 2023, ApJ, 952, 142
Gaia Collaboration, Vallenari, A., Brown, A. G. A., et al. 2023, A&A, 674, A1
Gehrels, N. 1986, ApJ, 303, 336
Goulding, A. D., Greene, J. E., Setton, D. J., et al. 2023, ApJL, 955, L24
Greene, J. E., Labbe, I., Goulding, A. D., et al. 2024, ApJ, 964, 39
GREX-PLUS Science Team, Inoue, A. K., Harikane, Y., et al. 2023, arXiv:2304.08104
Grogin, N. A., Kocevski, D. D., Faber, S. M., et al. 2011, ApJS, 197, 35
Grudić, M. Y., Hopkins, P. F., Quataert, E., & Murray, N. 2019, MNRAS, 483, 5548
Hainline, K. N., Maiolino, R., Juodžbalis, I., et al. 2025, ApJ, 979, 138
Harikane, Y., Inoue, A. K., Ellis, R. S., et al. 2025, ApJ, 980, 138
Harikane, Y., Inoue, A. K., Mawatari, K., et al. 2022b, ApJ, 929, 1
Harikane, Y., Ono, Y., Ouchi, M., et al. 2022a, ApJS, 259, 20
Harikane, Y., Ouchi, M., Oguri, M., et al. 2023b, ApJS, 265, 5
Harikane, Y., Zhang, Y., Nakajima, K., et al. 2023a, ApJ, 959, 39
Harish, S., Kartaltepe, J. S., Liu, D., et al. 2025, ApJ, 992, 45
Heintz, K. E., Watson, D., Brammer, G., et al. 2024, Sci, 384, 890

Helton, J. M., Rieke, G. H., Alberts, S., et al. 2025, NatAs, 9, 729
Hopkins, P. F., Murray, N., Quataert, E., & Thompson, T. A. 2010, MNRAS, 401, L19
Hviding, R. E., de Graaff, A., Miller, T. B., et al. 2025, A&A, 702, A57
Inayoshi, K. 2025, ApJL, 988, L22
Inayoshi, K., & Ichikawa, K. 2024, ApJL, 973, L49
Inayoshi, K., Kimura, S., & Noda, H. 2025, PASJ, 77, 811
Inayoshi, K., & Maiolino, R. 2025, ApJL, 980, L27
Inayoshi, K., Onoue, M., Sugahara, Y., Inoue, A. K., & Ho, L. C. 2022, ApJL, 931, L25
Inayoshi, K., Shangguan, J., Chen, X., Ho, L. C., & Haiman, Z. 2025, arXiv:2505.05322
Inoue, A. K. 2011, MNRAS, 415, 2920
Inoue, A. K., Yamamura, I., Suzuki, T., et al. 2024, Proc. SPIE, 13092, 130920Y
Ji, X., D'Eugenio, F., Juodžbalis, I., et al. 2025a, arXiv:2507.23774
Ji, X., Maiolino, R., Übler, H., et al. 2025b, MNRAS, in press
Jiang, L., Kashikawa, N., Wang, S., et al. 2021, NatAs, 5, 256
Kido, D., Ioka, K., Hotokezaka, K., Inayoshi, K., & Irwin, C. M. 2025, MNRAS, in press
Killi, M., Watson, D., Brammer, G., et al. 2024, A&A, 691, A52
Kocevski, D. D., Finkelstein, S. L., Barro, G., et al. 2025, ApJ, 986, 126
Kocevski, D. D., Onoue, M., Inayoshi, K., et al. 2023, ApJL, 954, L4
Koekemoer, A. M., Aussel, H., Calzetti, D., et al. 2007, ApJS, 172, 196
Koekemoer, A. M., Faber, S. M., Ferguson, H. C., et al. 2011, ApJS, 197, 36
Kokorev, V., Caputi, K. I., Greene, J. E., et al. 2024a, ApJ, 968, 38
Kokorev, V., Chisholm, J., Endsley, R., et al. 2024b, ApJ, 975, 178
Kokubo, M., & Harikane, Y. 2024, arXiv:2407.04777
Kovács, O. E., Bogdán, Á., Natarajan, P., et al. 2024, ApJL, 965, L21
Kulkarni, G., Worseck, G., & Hennawi, J. F. 2019, MNRAS, 488, 1035
Kümmel, M., Bertin, E., Schefer, M., et al. 2020, in ASP Conf. Ser. 527, Astronomical Data Analysis Software and Systems XXIX, ed. R. Pizzo et al. (San Francisco, CA: ASP), 29
Labbé, I., van Dokkum, P., Nelson, E., et al. 2023, Natur, 616, 266
Labbe, I., Greene, J. E., Bezanson, R., et al. 2025, ApJ, 978, 92
Labbe, I., Greene, J. E., Matthee, J., et al. 2024, arXiv:2412.04557
Lambrides, E., Garofali, K., Larson, R., et al. 2024, arXiv:2409.13047
Laor, A. 1998, ApJL, 505, L83
Li, W., Inayoshi, K., Onoue, M., et al. 2024, ApJ, 969, 69
Lin, R., Zheng, Z.-Y., Jiang, C., et al. 2025, ApJL, 980, L34
Lin, X., Fan, X., Cai, Z., et al. 2025b, arXiv:2507.10659
Lin, X., Fan, X., Wang, F., et al. 2025a, arXiv:2504.08039
Liu, H., Jiang, Y.-F., Quataert, E., Greene, J. E., & Ma, Y. 2025, ApJ, 994, 113
Lusso, E., & Risaliti, G. 2016, ApJ, 819, 154
Ma, Y., Greene, J. E., Setton, D. J., et al. 2025a, ApJ, 981, 191
Ma, Y., Greene, J. E., Setton, D. J., et al. 2025b, arXiv:2504.08032
Madau, P., & Haardt, F. 2024, ApJL, 976, L24
Maiolino, R., Risaliti, G., Signorini, M., et al. 2025, MNRAS, 538, 1921
Maiolino, R., Scholtz, J., Curtis-Lake, E., et al. 2024a, A&A, 691, A145
Maiolino, R., Scholtz, J., Witstok, J., et al. 2024b, Natur, 627, 59
Matsuoka, Y., Onoue, M., Kashikawa, N., et al. 2016, ApJ, 828, 26
Matthee, J., Naidu, R. P., Brammer, G., et al. 2024, ApJ, 963, 129
Mazzolari, G., Gilli, R., Maiolino, R., et al. 2024, arXiv:2412.04224
Naidu, R. P., Matthee, J., Katz, H., et al. 2025a, arXiv:2503.16596
Naidu, R. P., Oesch, P. A., Brammer, G., et al. 2025b, arXiv:2505.11263
Napolitano, L., Castellano, M., Pentericci, L., et al. 2025, A&A, 693, A50
Newman, S. L., Lovell, C. C., Maraston, C., et al. 2025, MNRAS, in press
Niida, M., Nagao, T., Ikeda, H., et al. 2020, ApJ, 904, 89
Norris, M. A., Kannappan, S. J., Forbes, D. A., et al. 2014, MNRAS, 443, 1151
Oesch, P. A., Brammer, G., van Dokkum, P. G., et al. 2016, ApJ, 819, 129
Oke, J. B., & Gunn, J. E. 1983, ApJ, 266, 713
Ono, Y., Ouchi, M., Harikane, Y., et al. 2025, ApJ, 991, 222
Onoue, M., Inayoshi, K., Ding, X., et al. 2023, ApJL, 942, L17
Pacucci, F., & Loeb, A. 2025, ApJL, 989, L19
Pacucci, F., & Narayan, R. 2024, ApJ, 976, 96
Parsa, S., Dunlop, J. S., & McLure, R. J. 2018, MNRAS, 474, 2904
Pérez-González, P. G., Costantin, L., Langeroodi, D., et al. 2023, ApJL, 951, L1
Pérez-González, P. G., Rinaldi, P., Caputi, K. I., et al. 2024, ApJL, 969, L10
Perger, K., Fogasy, J., Frey, S., & Gabányi, K. É. 2025, A&A, 693, L2
Pollock, C. L., Gottumukkala, R., Heintz, K. E., et al. 2025, arXiv:2506.15779
Rest, A., Pierel, J., Correnti, M., et al. 2023, arminrest/jhat: The JWST HST Alignment Tool (JHAT), v2, Zenodo, doi:10.5281/zenodo.7892935
Rieke, G. H., Alberts, S., Shivaei, I., et al. 2024, ApJ, 975, 83

Rieke, M. J., Kelly, D. M., Misselt, K., et al. 2023, PASP, 135, 028001
Rigby, J., Perrin, M., McElwain, M., et al. 2023, PASP, 135, 048001
Sacchi, A., & Bogdan, A. 2025, ApJL, 989, L30
Salpeter, E. E. 1964, ApJ, 140, 796
Schechter, P. 1976, ApJ, 203, 297
Schmidt, M. 1968, ApJ, 151, 393
Scholtz, J., Maiolino, R., D'Eugenio, F., et al. 2025, A&A, 697, A175
Scholtz, J., Witten, C., Laporte, N., et al. 2024, A&A, 687, A283
Schwarz, G. 1978, AnSta, 6, 461
Sérsic, J. L. 1963, BAAA, 6, 41
Setton, D. J., Greene, J. E., de Graaff, A., et al. 2024, arXiv:2411.03424
Setton, D. J., Greene, J. E., Spilker, J. S., et al. 2025, ApJL, 991, L10
Shen, X., Hopkins, P. F., Faucher-Giguère, C.-A., et al. 2020, MNRAS, 495, 3252
Shen, Y. 2013, BASI, 41, 61
Shen, Y., Richards, G. T., Strauss, M. A., et al. 2011, ApJS, 194, 45
Shuntov, M., Akins, H. B., Paquereau, L., et al. 2025, arXiv:2506.03243
Smolčić, V., Novak, M., Bondi, M., et al. 2017, A&A, 602, A1
Stetson, P. B. 1987, PASP, 99, 191
Tanaka, T. S., Silverman, J. D., Ding, X., et al. 2025, ApJ, 979, 215
Tanaka, T. S., Silverman, J. D., Shimasaku, K., et al. 2024, arXiv:2412.14246
Taylor, A. J., Finkelstein, S. L., Kocevski, D. D., et al. 2025a, ApJ, 986, 165
Taylor, A. J., Kokorev, V., Kocevski, D. D., et al. 2025b, ApJL, 989, L7
Tee, W. L., Fan, X., Wang, F., & Yang, J. 2025, ApJL, 983, L26
Temple, M. J., Hewett, P. C., & Banerji, M. 2021, MNRAS, 508, 737
Ueda, Y., Akiyama, M., Hasinger, G., Miyaji, T., & Watson, M. G. 2014, ApJ, 786, 104
Vestergaard, M., & Peterson, B. M. 2006, ApJ, 641, 689
Wang, B., de Graaff, A., Davies, R. L., et al. 2025, ApJ, 984, 121
Wang, F., Yang, J., Fan, X., et al. 2021, ApJL, 907, L1
Wang, F., Yang, J., Hennawi, J. F., et al. 2023, ApJL, 951, L4
Williams, C. C., Alberts, S., Ji, Z., et al. 2024, ApJ, 968, 34
Willott, C. J., Delorme, P., Reylé, C., et al. 2010, AJ, 139, 906
Withers, S., Muzzin, A., Ravindranath, S., et al. 2023, ApJL, 958, L14
Wu, Z., Eisenstein, D. J., Johnson, B. D., et al. 2025, ApJ, 992, 212
Wuyts, S., Franx, M., Cox, T. J., et al. 2009, ApJ, 696, 348
Yang, J., Fan, X., Gupta, A., et al. 2023, ApJS, 269, 27
Yue, M., Eilers, A.-C., Ananna, T. T., et al. 2024, ApJL, 974, L26
Zavala, J. A., Castellano, M., Akins, H. B., et al. 2025, NatAs, 9, 155
Zhang, Z., Jiang, L., Liu, W., & Ho, L. C. 2025a, ApJ, 985, 119
Zhang, Z., Jiang, L., Liu, W., Ho, L. C., & Inayoshi, K. 2025b, arXiv:2506.04350
Zhou, S., Sun, M., Zhang, Z., Chen, J., & Ho, L. C. 2025, ApJ, 991, 137
Zhuang, M.-Y., Li, J., Shen, Y., et al. 2025, arXiv:2505.20393